Monthly Notices of the ROYAL ASTRONOMICAL SOCIETY
MNRAS **482,** 2336–2353 (2019)

doi:10.1093/mnras/sty2724

Multifrequency study of the gamma-ray flaring BL Lacertae object PKS 2233–148 in 2009–2012

A. B. Pushkarev [1,2]★ M. S. Butuzova,[1] Y. Y. Kovalev[2,3,4] and T. Hovatta[5]

[1]*Crimean Astrophysical Observatory, Nauchny 298409, Crimea, Russia*
[2]*Astro Space Center of Lebedev Physical Institute, Profsoyuznaya 84/32, Moscow 117997, Russia*
[3]*Moscow Institute of Physics and Technology, Dolgoprudny, Institutsky per. 9, Moscow region 141700, Russia*
[4]*Max-Planck-Institut für Radioastronomie, Auf dem Hügel 69, 53121 Bonn, Germany*
[5]*Tuorla Observatory, Department of Physics and Astronomy, University of Turku, FI-20014 Turku, Finland*

Accepted 2018 October 3. Received 2018 October 1; in original form 2018 August 17

ABSTRACT

We study the jet physics of the BL Lacertae object PKS 2233−148, making use of the synergy of observational data sets in the radio and γ-ray energy domains. The four-epoch multifrequency (4–43 GHz) very-long-baseline array (VLBA) observations focused on the parsec-scale jet were triggered by a flare in γ-rays registered by *Fermi*-LAT on 2010 April 23. We also used 15-GHz data from the OVRO 40-m telescope and MOJAVE VLBA monitoring programs. The jet shape of the source is found to be conical on scales probed by the VLBA observations, setting a lower limit of about 0.1 on its unknown redshift. Nuclear opacity is dominated by synchrotron self-absorption, with a wavelength-dependent core shift of $r_{\rm core\,[mas]} \approx 0.1\lambda_{\rm [cm]}$ mas co-aligned with the innermost jet direction. The turnover frequency of the synchrotron spectrum of the very-long-baseline interferometry core shifts towards lower frequencies as the flare propagates down the jet, and the speed of this propagation is significantly higher, about 1.2 mas yr^{-1}, than results from traditional kinematics based on tracking bright jet features. We have found indications that the γ-ray production zone in the source is located at large distances, 10–20 pc, from a central engine, and could be associated with the stationary jet features. These findings favour synchrotron self-Compton, possibly in combination with external Compton scattering by infrared seed photons from a slow sheath of the jet, as the dominant high-energy emission mechanism of the source.

Key words: galaxies: active – galaxies: jets – gamma-rays: galaxies – BL Lacertae objects: individual: PKS 2233–148.

1 INTRODUCTION

The location of the γ-ray production zone in active galactic nuclei (AGNs) is still an open and actively debated question. The limited angular resolution of γ-ray telescopes means that it is impossible to directly locate the region responsible for the high-energy emission in AGNs. A variety of approaches have been considered to address this problem, and our current understanding is that the regions of γ-ray production may be at different locations in different sources, as is evident from observations. One of the two main competing scenarios is based on the observed rapid γ-ray variability on time-scales of a few hours and suggests that the high-energy emission from blazars is generated on subparsec scales, near the central black hole (e.g. Tavecchio et al. 2010; Yan et al. 2018). Similarly, the observed strength and variability of the absorption of the γ-ray emission in the blazar 3C 454.3 suggests that the γ-ray-emitting zone is within the broad-line region (Bai, Liu & Ma 2009; Poutanen & Stern 2010). The second scenario, in contrast, concludes that the dominant population of γ-ray photons is produced at larger, parsec scales, at distances up to 10–20 pc (Marscher et al. 2010; Agudo et al. 2011; Schinzel et al. 2012; Fuhrmann et al. 2016; Karamanavis et al. 2016), and is based on a joint analysis of data in the γ-ray and radio bands. Kovalev et al. (2009) and Pushkarev, Kovalev & Lister (2010) showed that variability in γ-rays leads that of the 15-GHz radio core on a time-scale of up to a few months. In this paper we are concerned with one particular AGN, the BL Lac object 2233 − 148, which was observed during and after the flare in γ-rays registered in 2010 April by *Fermi*-LAT.

The structure of the paper is as follows: in Section 2 we describe our and archival observational data and reduction schemes; in Section 3 we discuss our results; and our main conclusions are summarized in Section 4. We use the term 'core' to denote the apparent origin of AGN jets, which commonly appears as the brightest fea-

★ E-mail: pushkarev.alexander@gmail.com

Table 1. Frequency set-up for the S2087D VLBA experiment.

Band	Frequency channels			
	IF1 [MHz]	IF2 [MHz]	IF3 [MHz]	IF4 [MHz]
C	4600.5	4608.5	4995.5	5003.5
X	8100.5	8108.5	8421.5	8429.5
U	15349.5	15357.5	15365.5	15373.5
K	23788.5	23796.5	23804.5	23812.5
Q	43201.5	43209.5	43217.5	43225.5

ture in very-long-baseline interferometry (VLBI) images of blazars (e.g. Lobanov 1998). The spectral index α is defined as $S_\nu \propto \nu^\alpha$, where S_ν is the observed flux density at frequency ν. All position angles are given in degrees east of north. We adopt a cosmology with $\Omega_\mathrm{m} = 0.27$, $\Omega_\Lambda = 0.73$ and $H_0 = 71$ km s^{-1} Mpc^{-1} (Komatsu et al. 2009).

2 OBSERVATIONS AND DATA PROCESSING

2.1 Multi-epoch 4.6–43.2 GHz VLBA observations

For the purposes of our study, we made use of data on the BL Lac object PKS 2233 − 148 as observed (code S2087D) with the very-long-baseline array (VLBA) of the National Radio Astronomy Observatory (NRAO) during four sessions at epochs 2010 May 15, 2010 June 25, 2010 August 1 and 2010 September 9. All 10 VLBA antennas participated in each experiment. The observations were performed in a full polarimetric mode simultaneously in the C, X, U, K and Q frequency bands, which correspond to 6-, 4-, 2-, 1.3- and 0.7-cm wavelengths, respectively (Table 1). Each band was separated into four 8-MHz-wide intermediate frequency channels (IFs), with 16 spectral channels per IF. The signal was recorded with 2-bit sampling at a total recording rate of 256 Mbps with an analogue base-band converter. The data were correlated at the NRAO VLBA Operations Center in Socorro (New Mexico, USA) with an averaging time of 2 s. We split the C and X bands into two subbands (each of 16 MHz width) centred at 4608.5, 5003.5 MHz and 8108.5, 8429.5 MHz, respectively, and in the subsequent analysis the data were processed independently. The U, K and Q bands were not split into subbands, resulting in 32-MHz bandwidths centred at 15365.5, 23804.5 and 43217.5 MHz. The on-source time at each epoch was, in total, about 45 min for the C and X bands, 53 min for the U and K bands, and 83 min the Q band, split into 12 scans distributed over 8 h. The scans were scheduled over a number of different hour angles to maximize the (u, v) plane coverage. The increase of the on-source time with frequency was scheduled with the aim of obtaining comparable image sensitivity at all bands.

The data reduction was performed with the NRAO Astronomical Image Processing System (AIPS, Greisen 2003) following the standard procedure. The individual IFs for each frequency band were processed separately throughout the data reduction. The antenna gain curves and system temperatures measured during the sessions were used for a priori amplitude calibration. Global gain correction factors for each station for each IF were derived from the results of self-calibration. We applied the significant amplitude scale corrections listed in Table 2 by running the AIPS task CLCOR. The phase corrections for station-based residual delays and delay rates were found and applied using the AIPS task FRING in two steps. First, the manual fringe-fitting was run on a short interval on a bright quasar, 3C 454.3 (2251 + 158), in order to determine the relative instrumental phase and residual group delay for each individual IF. Secondly, the global fringe-fitting was run by specifying a point-like source model and a signal-to-noise ratio cutoff of 5 to omit noisy solutions. The fringe-fit solution interval was chosen to be 10, 4, 2, 1.5 and 1 min for the C, X, U, K and Q band, respectively. After fringe-fitting, a complex bandpass calibration was made. The estimated accuracy of the VLBA amplitude calibration in the 5–15 GHz frequency range is about 5 per cent, and at 24–43 GHz is about 10 per cent (see also Kovalev et al. 2005; Sokolovsky et al. 2011).

Table 2. Amplitude scale corrections for the S2087D VLBA experiment. The full table is available online.

Antenna (1)	Band (2)	Epoch (3)	IF (4)	Correction (5)
BR	K	1	1–2	0.88
BR	K	1	3–4	0.85
BR	K	2,3,4	1–4	0.80
FD	U	1	1–4	1.09
FD	Q	1	1–4	1.15
KP	C	2,4	1–2	1.08

CLEANing (Högbom 1974), phase and amplitude self-calibration (Jennison 1958; Twiss, Carter & Little 1960) and hybrid imaging (Readhead et al. 1980; Schwab 1980; Cornwell & Wilkinson 1981) were performed in the Caltech DIFMAP (Shepherd 1997) package. A point-source model was used as an initial model for the iterative procedure. Final maps were produced by applying a natural weighting of the visibility function. The spanned bandwidth of the IFs in each band is small (<0.2 per cent of the fractional bandwidth in all bands), and thus no spectral correction technique was applied.

In this paper, we present results inferred from the total-intensity images. The polarization calibration and results will be published in a separate paper.

2.2 Multi-epoch 15.4-GHz MOJAVE observations

We also made use of the data at 15.4 GHz from the MOJAVE (Monitoring of Jets in Active Galactic Nuclei With VLBA Experiments) program.[1] The data were obtained at eight more epochs at 15.4 GHz: 2009-12-26, 2010-06-19, 2010-12-24, 2011-09-12, 2012-05-24, 2012-07-12, 2012-12-10 and 2016-09-17. We used the fully calibrated publicly available data. For a more detailed discussion of the data reduction and imaging process schemes, see Lister et al. (2018). The absolute flux density of the observations is accurate within 5 per cent (Lister & Homan 2005; Hovatta et al. 2012).

2.3 15-GHz OVRO observations

We also used public data[2] for PKS 2233 − 148 observations performed within the Owens Valley Radio Observatory 40-m Telescope monitoring program (Richards et al. 2011). Observations were carried out at 15 GHz in a 3-GHz bandwidth from 2008-10-23 to 2018-02-05 with a typical time sampling of about 4 d. Details of the data reduction and calibration are given in Richards et al. (2011).

[1] http://www.astro.purdue.edu/MOJAVE
[2] http://www.astro.caltech.edu/ovroblazars

2.4 γ-ray *Fermi*-LAT data

The γ-ray light-curve was generated from data obtained with the LAT (Atwood et al. 2009) onboard the *Fermi* γ-ray space telescope between 2008-08-09 and 2016-10-17. In the analysis, we used the *Fermi* SCIENCETOOLS software package[3] version v10r0p5 and Pass 8 data. In order to generate the light-curve, we first selected all photons between 100 MeV and 300 GeV within a 10° region of interest (ROI) around the source. In the event selection and analysis we followed the recommendations for Pass 8 data given by the LAT team.[4]

The photon flux over each 7-d bin was calculated using the tool *gtlike* with instrument response function version P8R2_SOURCE_V6. The source model was generated using the external tool make3FGLxml.py version 01 by selecting all sources within 20° of the target in the 3FGL catalogue (Acero et al. 2015), and also including the Galactic diffuse emission model version *gll_iem_v06* and the isotropic diffuse emission model version *iso_source_v06*. Based on the 3FGL catalogue, the target was modelled with a log-parabola spectrum, defined as $\mathrm{d}N/\mathrm{d}E = N_0(E/E_b)^{-(\alpha+\beta\log(E/E_b))}$. In order to account for the low number of photons in each weekly bin and to reduce the number of free parameters in the fit, we froze the spectral parameters of the target and all other sources in the model to the values reported in 3FGL. For the target, the 3FGL values are $\alpha = 2.04$, $\beta = 0.09$ and $E_b = 581.68$. In addition, if the source was beyond the 10° ROI or had a test statistic (TS) value (e.g. Mattox et al. 1996) less than 5 in 3FGL, we also froze the flux to the value reported in 3FGL. If the TS of the bin was less than 4 (corresponding to about 2σ) or if the number of predicted photons in that bin was less than 10, we calculated a 95 per cent upper limit of the photon flux (Abdo et al. 2011).

3 RESULTS

3.1 Parsec-scale jet structure

Final naturally weighted VLBA maps of the source brightness distribution at the seven frequencies at each of the four observing epochs are presented in Fig. 1. The source shows a typical parsec-scale AGN morphology of a bright compact core and one-sided jet, which propagates towards the east and is detected up to a distance of about 2 mas at 43 GHz and progressively farther, up to 8 mas, at lower (4.6, 5.0 GHz) frequencies owing to the steep spectrum of the jet emission (see the more detailed discussion in Section 3.6). At the frequency of 8 GHz and higher, the outer jet regions are transversely resolved. The lower-frequency images show a faint emission beyond the core, probably caused by the uncompensated side-lobes owing to the low declination of the source. The images at 8 GHz are the most sensitive, with a typical noise level of about 0.16 mJy beam^{-1} and a dynamic range of the order of 3000, determined as the ratio of the peak flux density to the rms noise level. The noise level was calculated as the average of rms estimates in three corner quadrants of the image, each of 1/16 of the map size. The fourth quadrant, with a maximum rms, was excluded as being affected by the source structure. The achieved image noise levels are close to the thermal noise estimated for natural data weighting. In Table 3, we summarize the VLBA map parameters.

[3]http://fermi.gsfc.nasa.gov/ssc/data/analysis/documentation/Cicerone
[4]http://fermi.gsfc.nasa.gov/ssc/data/analysis/documentation/Pass8_usage.html

Structure modelling of the source brightness distribution was performed with the procedure *modelfit* in the DIFMAP package by fitting several circular Gaussian components to the calibrated visibility data and minimizing χ^2 in the spatial frequency plane. We used a minimum number of components (three at lower and four at higher frequencies) that, after being convolved with the restoring beam, adequately reproduce the constructed source morphology. The obtained source models are listed in Table 4 and provide flux densities, positions and sizes of the fitted components. All the positions are given with respect to the core component.

3.2 Radio and γ-ray light-curves

In Fig. 2, we present light-curves of PKS 2233 − 148 based on the *Fermi*-LAT and OVRO monitoring data, complemented by measurements from the MOJAVE program and our VLBA observations at 15 GHz. The prominent variability at high energies detected during 2010 April and June triggered the four-epoch VLBA multifrequency campaign. The values of the correlated VLBA total flux density are in good agreement with the single-dish OVRO flux density measurements, implying that there is almost no extended emission on kiloparsec scales, as was previously concluded by Drinkwater et al. (1997). We performed a cross-correlation analysis of the light-curves using the z-transformed discrete correlation function (Alexander 1997), specifically developed for sparse, unevenly sampled light-curves. The correlation between the radio and γ-ray light-curves with and without upper limits is insignificant, suggesting that the γ-ray production region in the source might have a complex structure. We discuss this in more detail in Section 3.9.

3.3 Core shifts

The VLBI core is believed to represent the apparent jet starting region, located at a distance $r_{\rm core}$ from the central engine, at which its optical depth reaches $\tau_\nu \approx 1$ at a given frequency. Thus, as a result of nuclear opacity, the absolute position of the radio core is frequency-dependent and varies as $r_{\rm core} \propto \nu^{-1/k_{\rm r}}$ (Blandford & Königl 1979; Konigl 1981). There is growing observational evidence from recent multifrequency studies of the core-shift effect for $k_{\rm r} \approx 1$ (e.g. O'Sullivan & Gabuzda 2009; Fromm et al. 2010; Sokolovsky et al. 2011; Hada et al. 2011; Kravchenko et al. 2016; Lisakov et al. 2017). This is consistent with the Blandford & Königl (1979) model of a synchrotron self-absorbed conical jet in equipartition between energy densities of the magnetic field and the radiating particles. Departures in $k_{\rm r}$ from unity are also possible (Kutkin et al. 2014, Plavin et al. 2018) and can be caused by pressure and density gradients in the jet or by external absorption from the surrounding medium (Lobanov 1998; Kadler et al. 2004).

We calculated the core-shift vector as $\boldsymbol{\Delta r}_{{\rm core},\nu_1\nu_2} = \boldsymbol{\Delta r}_{12} - (\boldsymbol{r}_1 - \boldsymbol{r}_2)$, where $\boldsymbol{\Delta r}_{12}$ is the displacement of the phase centres of the images at different frequencies, and $\boldsymbol{r}_1$, $\boldsymbol{r}_2$ are VLBI core-position offsets from the phase centre. In order to derive the image shift vector $\boldsymbol{\Delta r}_{12}$, we used the fast normalized cross-correlation algorithm (Lewis 1995) to align the images to the same position on the sky, selecting the jet regions of optically thin emission and assuming that their positions are achromatic. Every pair of images was restored with the average beam size using a pixel size of 0.03 mas.

In Fig. 3, we present a plot of 65 derived core-shift vectors, where the head of each vector represents the core position at lower frequency, while all core positions at higher frequency of a pair are

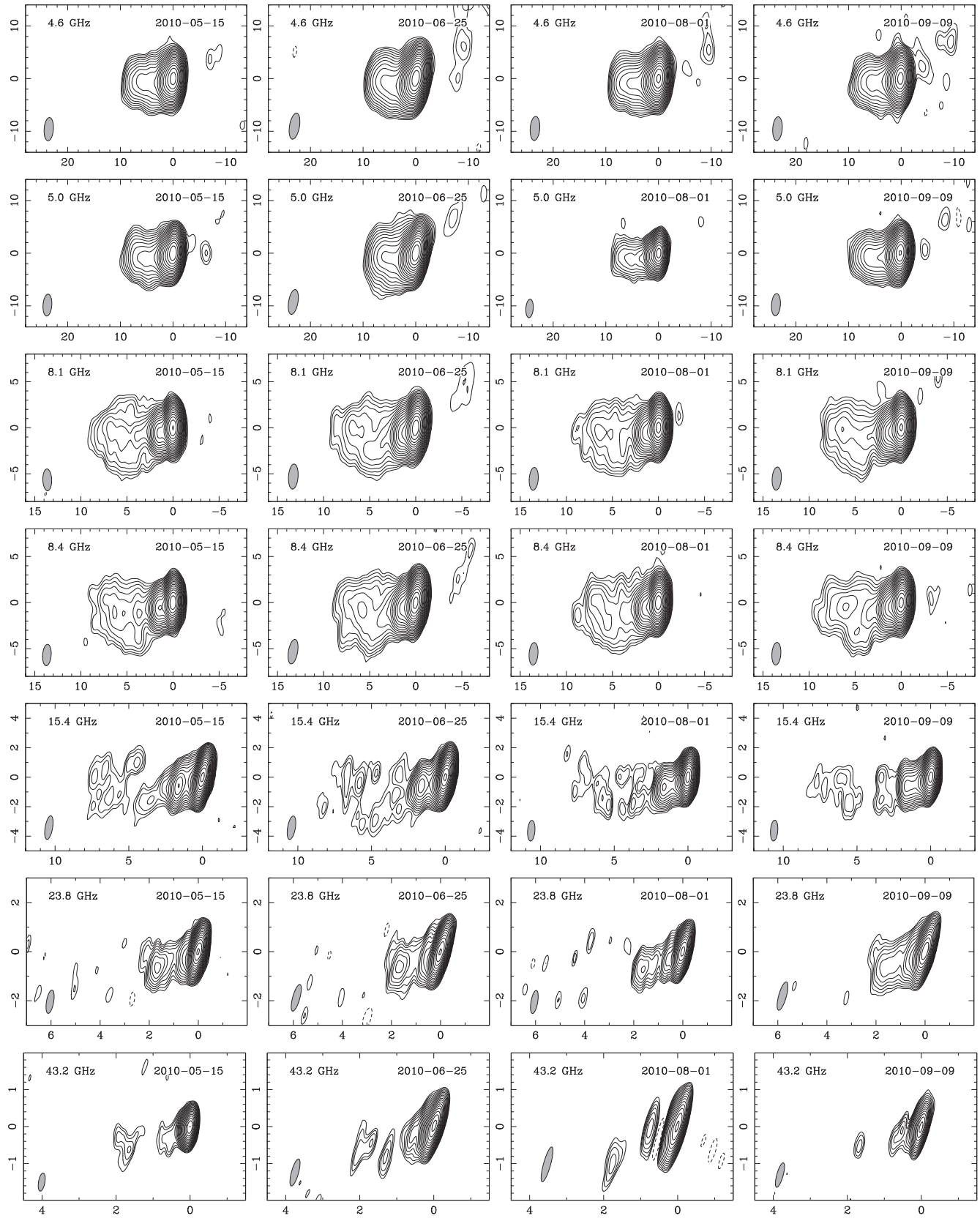

Figure 1. Naturally weighted total-intensity contour maps of PKS 2233−148 at four epochs during 2010 at 4.6, 5.0, 8.1, 8.4, 15.4, 23.8 and 43.2 GHz, with a cell size of 0.3, 0.3, 0.2, 0.2, 0.1, 0.06 and 0.03 mas per pixel, respectively. The *x*- and *y*-axes are given in mas of relative right ascension and relative declination, respectively. The contours are plotted at increasing powers of $\sqrt{2}$ starting from the 4 rms level. The full-width at half maximum (FWHM) of the restoring beam is shown as a shaded ellipse in the lower left corner. Note that the scales in the different images are different. The image parameters are listed in Table 3.

Table 3. Summary of image parameters. Columns are as follows: (1) epoch of observations, (2) central observing frequency, (3) *I* peak of image, (4) rms noise level of image, (5) theoretical thermal noise estimate, (6) bottom *I* contour level, (7) dynamic range of image, (8) total flux density from map, (9) full-width at half maximum (FWHM) major axis of restoring beam, (10) FWHM minor axis of restoring beam, (11) position angle of major axis of restoring beam. The full table is available online.

Epoch	Freq.	$I_{\rm peak}$	$I_{\rm rms}$	Thermal noise	$I_{\rm base}$	DR	$S_{\rm VLBA}$	$B_{\rm maj}$	$B_{\rm min}$	$B_{\rm PA}$
	[GHz]	[mJy bm^{-1}]	[mJy bm^{-1}]	[mJy bm^{-1}]	[mJy bm^{-1}]		[mJy]	[mas]	[mas]	[°]
(1)	(2)	(3)	(4)	(5)	(6)	(7)	(8)	(9)	(10)	(11)
2010–05–15	4.608	335	0.19	0.11	0.76	1756	505	4.40	1.74	−2.0
2010–06–25	4.608	408	0.15	0.11	0.61	2676	569	4.97	1.87	−7.6
2010–08–01	4.608	382	0.17	0.11	0.68	2235	538	4.54	1.80	−3.5
2010–09–09	4.608	357	0.21	0.11	0.83	1723	510	4.50	1.79	−2.0
2010–05–15	5.003	350	0.18	0.15	0.71	1979	519	4.14	1.65	−3.3
2010–06–25	5.003	413	0.15	0.15	0.60	2737	570	4.74	1.76	−8.1
2010–08–01	5.003	371	0.30	0.15	1.19	1243	542	3.51	1.39	−2.2

Table 4. Source models. Columns are as follows: (1) observation date, (2) name of the component, (3) flux density of the fitted Gaussian component, (4) position offset from the core component, (5) position angle of the component with respect to the core component, (6) full-width at half maximum (FWHM) of the fitted circular Gaussian, (7) signal-to-noise ratio of the fitted Gaussian. The full table is available online.

Date	Comp.	Flux density	Distance	P.A.	Size	SNR
		[Jy]	[mas]	[°]	[mas]	
(1)	(2)	(3)	(4)	(5)	(6)	(7)
			4.6 GHz			
2010–05–15	Core	0.304 ± 0.019	0.000	...	0.322 ± 0.014	535
	J2	0.127 ± 0.012	1.454 ± 0.036	113.7 ± 1.4	1.009 ± 0.070	207
	J1	0.068 ± 0.015	5.049 ± 0.515	100.5 ± 5.8	4.884 ± 1.030	23
2010–06–25	Core	0.363 ± 0.025	0.000	...	0.333 ± 0.016	428
	J2	0.127 ± 0.015	1.408 ± 0.048	114.2 ± 1.9	1.092 ± 0.094	134
	J1	0.068 ± 0.016	5.012 ± 0.557	103.0 ± 6.3	4.926 ± 1.114	20

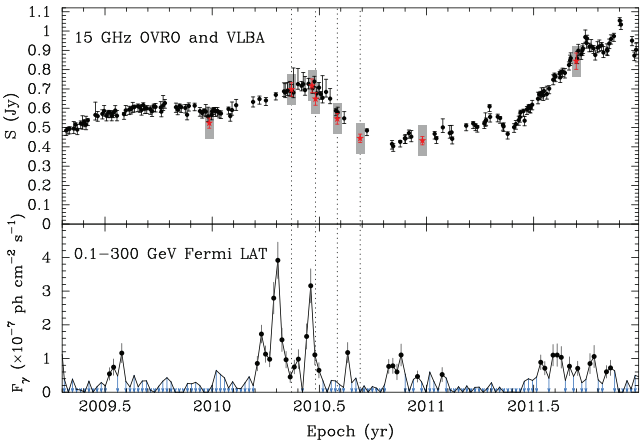

Figure 2. (Top) OVRO 15-GHz flux density evolution. Grey rectangles together with red stars indicate the VLBA total flux density at 15.4 GHz, observed within our campaign S2087D and the MOJAVE program. (Bottom) *Fermi* weekly binned γ-ray light-curve at 0.1–300 GeV. Upper limits are given by blue arrows. Dotted vertical lines indicate the epochs of the multifrequency VLBA observations.

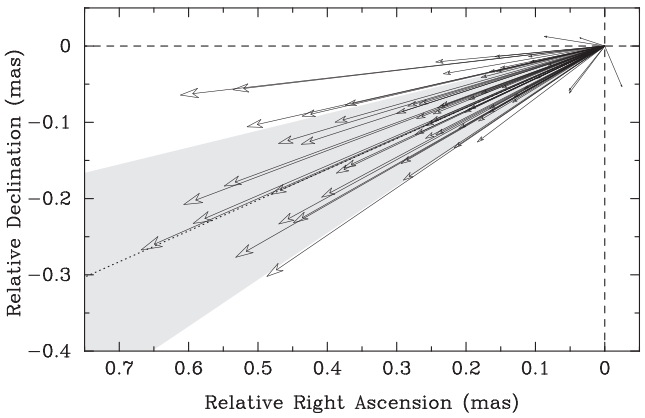

Figure 3. Core-shift vectors measured in all frequency pairs. The typical error is 0.045 mas. The shaded grey area encompasses 68 per cent of the vectors deviating by less than 10° from the median jet direction shown by the dotted line.

placed at the origin. The dotted line corresponds the median jet direction of P.A. = 112°. The core-shift effect occurs predominantly along the jet direction. In 68 per cent of cases, the core-shift vectors deviate by less than 10° from the median jet position angle. This good alignment is achievable for a relatively straight jet without substantial curvature in the core region. Assuming that the core shift takes place along the jet and that errors are random in direction, then the standard deviation of the transverse projections of the core-shift vectors on to the jet direction yields a typical error of 45 μas. Thus, in 90 per cent of cases the derived core shifts are significantly ($>2\sigma$) different from zero. In Table 5 we list the core-shift measurements: (1) epoch of observations, (2) pair of frequencies, (3) core-shift magnitude, (4) core-shift direction, (5) difference of observing wavelengths.

We studied the frequency dependence of the core shifts (Fig. 4) by fitting a function $\Delta r_{\rm core} = b(\nu^{-1/k_{\rm r}} - \nu_{\rm max}^{-1/k_{\rm r}})$, where b and $k_{\rm r}$ are fitted parameters, and $\nu_{\rm max}$ is fixed to the maximum frequency

Table 5. Core-shift vectors measured for the frequency pairs ν_1 and ν_2. The full table is available online.

Epoch	ν_1 ν_2 [GHz]	$\Delta r_{\mathrm{core},\nu_1\nu_2}$ [mas]	P.A. [°]	$\lambda_2 - \lambda_1$ [cm]
(1)	(2)	(3)	(4)	(5)
2010–05–15	43.2 23.8	0.038	73	0.566
2010–05–15	43.2 15.4	0.088	82	1.258
2010–05–15	43.2 8.4	0.278	106	2.865
2010–05–15	43.2 8.1	0.244	95	3.006
2010–05–15	43.2 5.0	0.539	96	5.302
2010–05–15	43.2 4.6	0.615	96	5.816
2010–05–15	23.8 15.4	0.078	138	0.692
2010–05–15	23.8 8.4	0.220	113	2.299

to which the core shifts were measured (43 GHz for the epochs 2010-05-15, 2010-06-25 and 2010-09-09; 23 GHz for the epoch 2010-08-01, at which we could not reliably measure the core shift with respect to the core position at 43 GHz). The fitted k_{r} values are smaller then but close to one and not significantly different from it. This can hold even during an outburst. As discussed in Plavin et al. (2018), a flare propagating down the jet disturbs only a limited portion of it, and thus k_{r} deviates from unity in a limited frequency range, which is significantly narrower than that of our observations. Therefore, for further analysis we use $k_{\mathrm{r}} = 1$. In this case, $r_{\mathrm{core}} \propto \lambda$. Following the approach proposed in Voitsik et al. (2018), in Fig. 5, we plot the measured core shifts against the difference in observing wavelengths (Table 5) and fit the dependence by a straight line, from which one can also estimate an offset of the apparent jet base at a given wavelength from the true jet origin by setting $\lambda_1 = 0$.

3.4 Jet shape

The core-shift measurements allow us to perform a jet geometry analysis for the whole set of the fitted components, including the cores. In Fig. 6, we plot the transverse jet widths d as the FWHM of the fitted Gaussian components at all four multifrequency VLBA epochs (Table 4) or the corresponding resolution limits (Kovalev et al. 2005), whichever is larger, as a function of their distance r from the true jet base taking into account the core-shift effect. The respective shifts $\Delta r_{\mathrm{core}} = a(t)\lambda$ were added to the fitted core separations, where $a(t)$ is the fitted slope at a corresponding observational epoch (Fig. 5). From this analysis we excluded 16 weak components with SNR < 15 to reduce the influence of low-SNR data points, although the whole set of 96 components yields qualitatively similar result. The BL Lac object PKS 2233 − 148 shows a conical streamline, with $d \propto r^{1.01 \pm 0.04}$ at scales probed by the multifrequency VLBA observations down to 0.1 mas. This is consistent with $k_{\mathrm{r}} \approx 1$ derived from the core-shift analysis.

The apparent jet-opening angle of the source is $38^\circ \pm 3^\circ$, as reported by Pushkarev et al. (2017), who measured it from a stacked total-intensity image at 15.4 GHz as a result of combining VLBA maps from 11 epochs distributed over a time range of about 3 yr, from 2009 to 2012. The wide opening angle suggests that the jet viewing angle is rather small, of the order of a few degrees.

3.5 Redshift constraint from the jet geometry

The optical spectrum of the source shows no prominent emission lines (Drinkwater et al. 1997) and its redshift is still unknown, but the inferred conical jet shape indicates that this BL Lac object is not too close, and probably located at a redshift exceeding ∼0.1. Otherwise, our VLBA observations would be sensitive enough to reveal a jet geometry transition from parabolic to conical shape, as we detect this transition in a number of nearby ($z \lesssim 0.1$) sources and explain it by a transition from a magnetically dominated to a particle-dominated regime in the outflows (Kovalev et al. 2018, in prep.). More distant AGNs ($z \gtrsim 0.1$) typically show close to conical jet streamlines (Pushkarev et al. 2017) because the scales probed by VLBI observations are beyond the shape-transition region.

3.6 Spectral index distribution

The procedure of image registration by means of 2D cross-correlation described in Section 3.3 allows us to align the images at different frequencies and accurately reconstruct a distribution of spectral index α over the source morphology. As an example, in Fig. 7 we present a spectral index map of PKS 2233 − 148 calculated between 4.6 and 23.8 GHz at the epoch 2010-09-09 of our multifrequency VLBA observations. The map shows that the core is partially opaque, with a spectral index of about 0.3, while the outer jet regions are optically thin, with a median value of $\alpha_{\mathrm{jet}} = -0.95$, which is typical for many other parsec-scale AGN jets (e.g. Pushkarev & Kovalev 2012; Hovatta et al. 2014). The spectral index error map manifests a higher α accuracy in the innermost jet area and progressively larger uncertainties towards regions with lower brightness, where random errors arising from the image noise dominate. Systematic errors (from image alignment) dominate in the core area, especially behind it. The same result was obtained statistically for a large sample of sources in our earlier paper (see Appendix B in Hovatta et al. 2014).

To analyse how the spectral index changes along the jet, we reconstructed the ridgeline of the outflow in total intensity using a procedure described in Pushkarev et al. (2017). As seen from Fig. 7 (bottom right), the spectral index along the ridgeline slightly flattens in the jet knots, indicating a reacceleration of emitting particles, while between them it is steeper. A similar behaviour was found to be typical in AGN jets (Pushkarev & Kovalev 2012; Hovatta et al. 2014).

The evolution of the spectral index along the ridgeline for all the frequency pairs (except for Q-band data) taken at all four epochs is presented in Fig. 8. Beyond the core region, the spectral index deviates around the value of about −1. The spectral index of optically thin synchrotron radiation parametrizes the energy spectrum of relativistic radiative particles. Assuming a power-law energy distribution $N(E) = N_0 E^{-s}$, the power index $s = 1 - 2\alpha$ has the mean value of ∼3.0. The evolution of α_{jet} down the jet shows no effect of spectral aging (steepening downstream) owing to radiative losses of relativistic electrons (Kardashev 1962), which is often seen in AGN jets on parsec scales (Pushkarev & Kovalev 2012). In the case of PKS 2233 − 148, the absence of this effect is probably caused by the dominance of a few quasi-stationary jet features, which could be standing shocks that effectively accelerate the emitting particles.

3.7 Synchrotron spectrum fitting and magnetic field estimates

For the spectral fitting of the core component (Table 4), we use the standard spectrum of a homogeneous incoherent synchrotron source of relativistic plasma with a power-law energy distribution of the form $N(E) \propto E^{-s}$ (Pacholczyk 1970):

$$S_\nu \propto \nu^{5/2} \left(1 - \exp\left[-\left(\frac{\nu_1}{\nu}\right)^{5/2-\alpha}\right]\right), \quad (1)$$

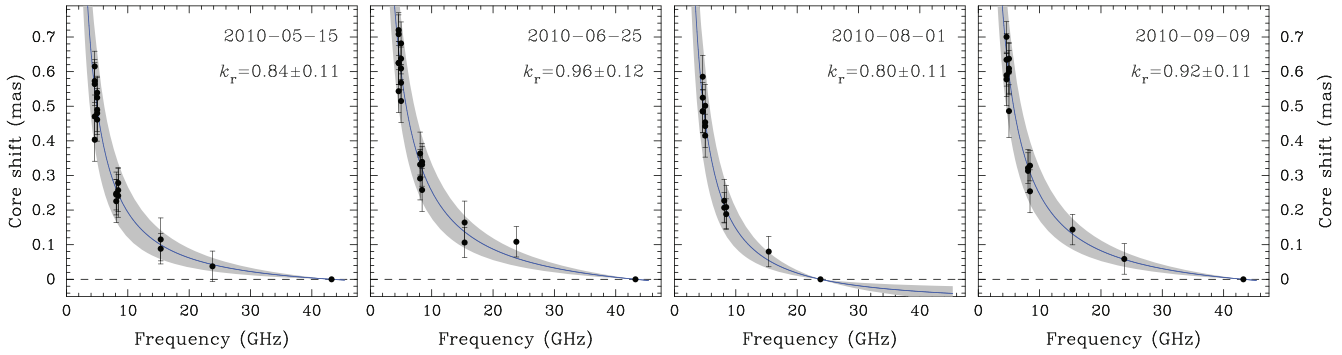

Figure 4. Frequency dependence of core shifts measured relative to the core position at 43 GHz (23 GHz for the epoch 2010-08-01) for all observational multifrequency epochs. Solid lines represent the best power-law fits. Shaded areas show 1σ confidence regions of the fit.

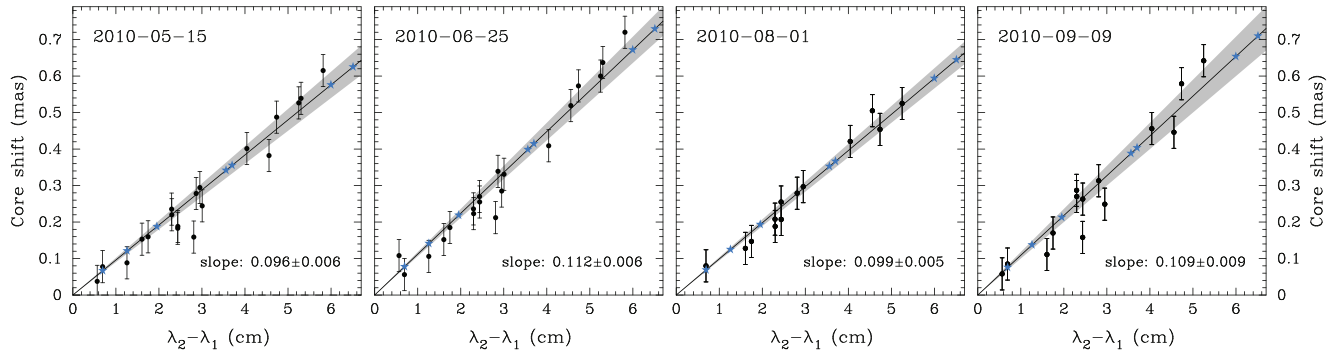

Figure 5. Core shifts as a function of difference of observing wavelengths. Solid lines represent the best linear fits. Shaded areas show 1σ confidence regions of the fit. Stars denote the expected core shifts from the true jet origin ($\lambda_1 = 0$) at the wavelengths of our observations, namely 0.7, 1.3, 2.0, 3.6, 3.7, 6.0 and 6.5 cm.

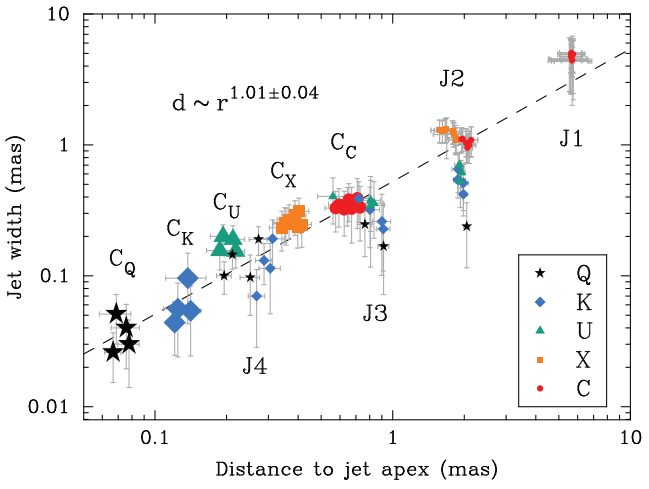

Figure 6. Jet width versus distance to the jet vertex for 78 components from structure model fits at seven frequencies for four epochs. Cores are marked by larger symbols. The dashed line is the best fit from the least-squares method. The jet shape at scales probed by our multi-frequency VLBA observations is conical.

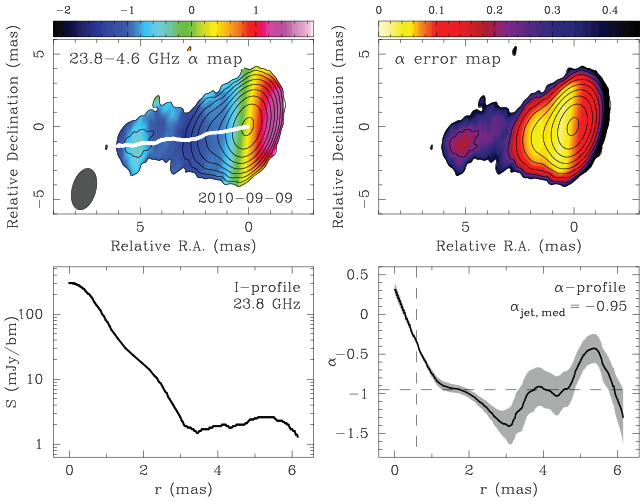

Figure 7. The distribution of the spectral index in PKS 2233−148 is shown in the top left panelat the epoch 2010 September 9 calculated between 4.6 and 23.8 GHz; it is shown in colour, with the 23.8-GHz total-intensity contours overlaid. The contours are plotted at increasing powers of 2, starting from 0.35 per cent of the peak brightness of 303 mJy beam^{-1}. The white curve denotes the total-intensity ridgeline. The restoring beam is depicted as a shaded ellipse in the lower left corner. The spectral index 1σ error map is shown in the top right panel. The bottom left and right panels show the total-intensity and spectral index profiles along the ridgeline, respectively. The vertical dashed line indicates the edge of the convolved VLBI core along the inner jet direction, while the horizontal dashed line represents the median jet spectral index. The grey area shows 1σ errors on the spectral index.

where ν_1 is the frequency at which the optical depth is $\tau = 1$. The fitted spectra of the core are presented in Fig. 9 (top). The best-fit parameters, namely the optically thin spectral index $\alpha = (1 - s)/2$, the peak flux density S_m and the corresponding self-absorption turnover frequency ν_m, are given for every spectrum. The core

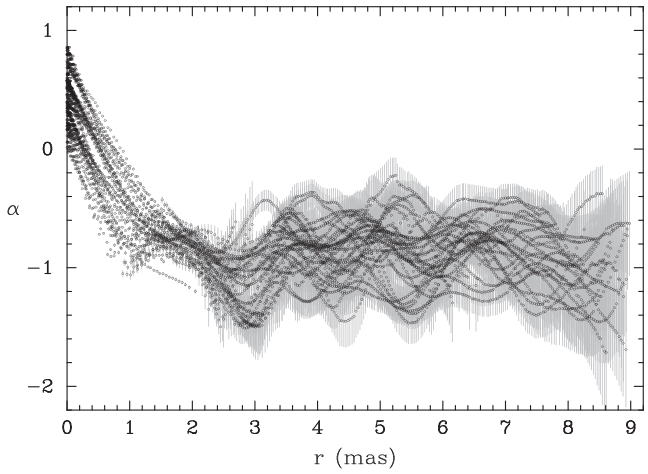

Figure 8. Spectral index evolution along the ridgeline for α-maps restored at all frequency pairs except the 43-GHz data. The grey bars show 1σ errors.

component shows a spectral turnover within the frequency range of our VLBA observations.

Using the fitted parameters $\nu_{\rm m}$, $S_{\rm m}$ and α of the synchrotron spectrum, we can estimate the magnetic field B within the source, adopting the standard synchrotron theory and assuming that the emission region is uniform and spherical. Then the commonly used expression for the component of the magnetic field perpendicular to the line of sight is (e.g. Marscher 1983; see Appendix A for more details)

$$B = 10^{-5}\, b(\alpha)\, \theta_{\rm m}^{4}\, \nu_{\rm m}^{5} S_{\rm m}^{\prime -2} \left(\frac{\delta}{1+z}\right) \quad [G], \tag{2}$$

where δ is the Doppler factor, z is the redshift, $\theta_{\rm m}$ is the diameter of the spherical component at the turnover frequency, $S'_{\rm m}$ is the flux density at $\nu_{\rm m}$ extrapolated from the straight-line optically thin slope, and $b(\alpha)$ (Fig. A1) is a function of the spectral index α, the optical depth $\tau_{\rm m}$ at $\nu_{\rm m}$, physical constants and a conversion factor, which allows one to express $\nu_{\rm m}$ in GHz, the angular size $\theta_{\rm m}$ in mas, and S'_m in Jy. To derive $\theta_{\rm m}$ we applied logarithmic interpolation between the measured component sizes at different frequencies (Table 4) and multiplied the result by a correction factor of 1.8 (Marscher 1987) to take into account that the emission feature is assumed to have a spherical shape, while performing model fitting we measure the FWHM of the circular Gaussian components. The flux density $S'_{\rm m}$ can be calculated using the following relationship:

$$S'_{\rm m} = S_{\rm m} {\rm e}^{\tau_{\rm m}}, \tag{3}$$

where the optical depth at the turnover can be derived numerically from the equation $\exp(\tau_{\rm m}) = 1 + \tau_{\rm m}(1 - 2\alpha/5)$ or approximated as (Türler, Courvoisier & Paltani 1999)

$$\tau = \frac{3}{2}\left(\sqrt{1 - \frac{16\alpha}{15}} - 1\right). \tag{4}$$

The mean value of the magnetic field inferred from equation (2) for the apparent core at the turnover frequency is $(0.03 \pm 0.01)\delta/(1 + z)$ G.

The only jet component detected at all the frequencies is J2 (see Fig. 6 and Table 4). It is located at a distance of about 2 mas from the core at 43 GHz. The spectra of this jet feature J2 in addition to a synchrotron fit were also fitted by a simple power law (Fig. 9, bottom). The spectrum of J2 is steep, with a spectral index gradually decreasing from about -1 to -1.6, while the turnover frequency increases slightly from 4.9 ± 0.4 to 5.9 ± 0.3 GHz.

3.8 Evolution of the turnover frequency and source kinematics

The self-absorption turnover frequency derived from the core spectra (Fig. 9, top) gradually decreases from 16.8 ± 5.3 GHz on 2010 May 15 to 6.4 ± 1.1 GHz on 2010 September 9, following an inverse proportionality to time ($\nu_{\rm m} \propto t^{-1}$), as predicted by a model of a conical jet with constant plasma speed (Blandford 1990). We interpret these changes as direct observational evidence of a flare propagating downstream. As a result of synchrotron opacity in the nuclear region, the flare developing along the jet becomes detectable at progressively larger distances from the true jet origin, corresponding to the VLBI core locations $r_{\rm core}$ at longer wavelengths. After the disturbance crosses the apparent core ($\tau \approx 1$ zone) at a given frequency, its flux density starts to decrease, resulting in a steepening of the core spectrum (Fig. 9, top) owing to energy losses to synchrotron radiation or Compton scattering (Kardashev 1962; Marscher & Gear 1985). The core offset from the jet apex can be calculated as $r_{\rm core} = r_{\rm flare} = a(t)\lambda_{\rm m}(t)$, where the parameter $a(t)$ was derived from the core-shift analysis for each epoch of the multifrequency VLBA observations (Fig. 5).

In Fig. 10, we show $r_{\rm flare}(\lambda_{\rm m})$ as a function of time. The slope of the weighted linear fit is 1.17 ± 0.10 mas yr^{-1}. The derived proper motion of the flare propagation is significantly higher than that inferred from a kinematics analysis based on tracing bright jet components. The two jet knots, J2 and J3, of the source studied within the MOJAVE program at 15 GHz are slow pattern features, with an angular speed of -71 ± 35 μas (apparent inward motion) and 45 ± 41 μas (Lister et al. 2016), respectively. These components are quasi-stationary and can be standing recollimation shocks observed in sources with super-magnetosonic jets (e.g. Asada & Nakamura 2012; Cohen et al. 2014) and also obtained in numerical 2D relativistic (magneto)-hydrodynamic simulations (Mizuno et al. 2015; Fromm 2015; Fuentes et al. 2018).

Because the jet geometry is found to be conical at scales probed by the VLBA observations (Section 3.4), we assume that the regime of constant flow speed holds at least up to 6 mas from the jet apex. Then the expected epoch for the flare to reach the quasi-stationary jet feature J2 at a distance of about 2 mas from the true jet base is $\sim$ 2012.0 (Fig. 10), at which the turnover frequency is expected to decrease to about 1.5 GHz. This scenario is supported by the flux-density evolution of the component at 15 GHz (Fig. 11). The component shows an increase of the flux density by a factor of about 2 during the period of time from $\sim$2011.5 to $\sim$2012.5. The epoch of the peak around 2012.0 was established by fitting the data with Gaussian process regression performed with the PyMC3 python module for Bayesian modelling, for which we used an exponential quadratic covariance function. Note that moving jet components behave in a completely different manner. Typically, their brightness rapidly fades as a result of energy losses and adiabatic expansion (e.g. Pushkarev & Kovalev 2012; Kravchenko et al. 2016; Lister et al. 2016).

It is therefore possible that the flare propagation rate represents the bulk flow speed. Taking into account the lower limit on redshift ($z > 0.49$) derived from the spectroscopy of the absorption lines formed by the intervening gas (Sbarufatti et al. 2006), the proper motion of the disturbance $\mu = 1.17 \pm 0.10$ mas yr^{-1} corresponds to an apparent speed of $\beta_{\rm app} > 34 \pm 2\,c$. This is much faster than the typical apparent speed of $\approx$4 c derived from a kinematics analysis for a sample of 42 BL Lacs and also significantly higher than

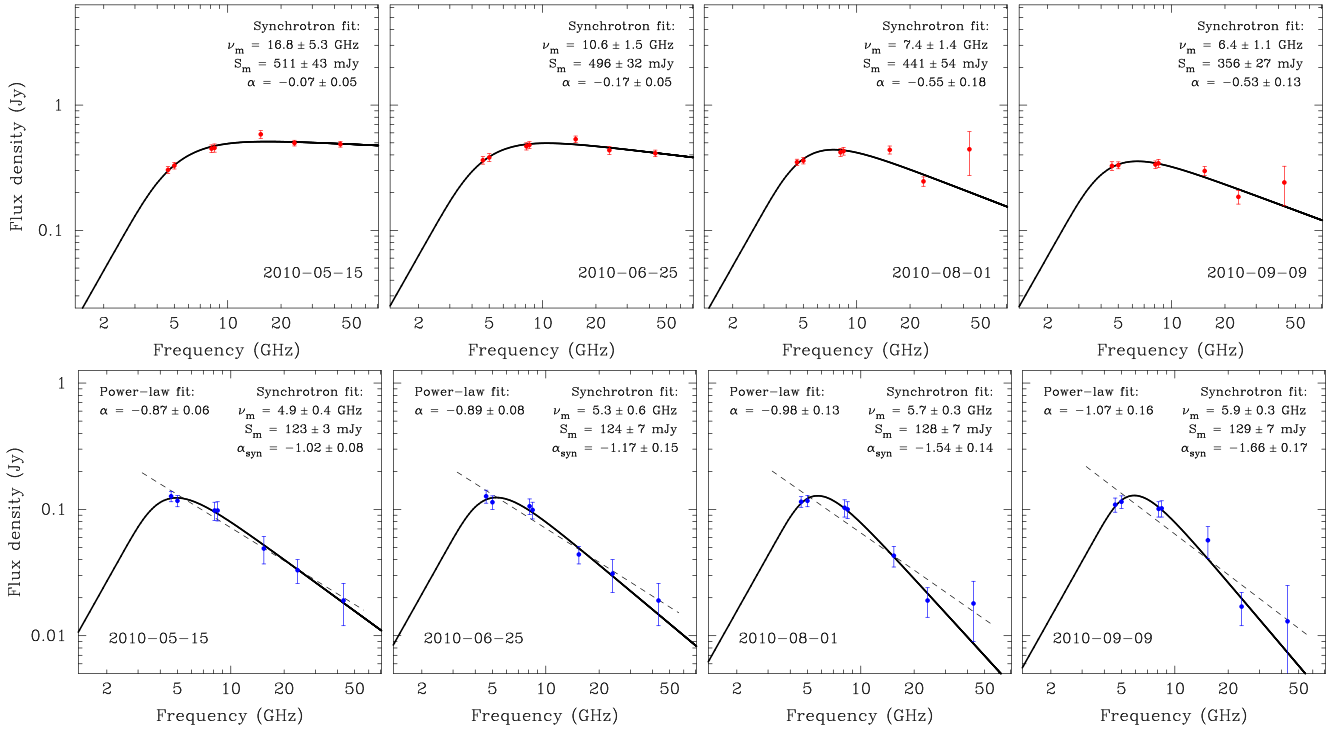

Figure 9. Spectral fits to the core (top) and jet feature J2 (bottom) data. Solid lines represent the spectra derived from the homogeneous synchrotron source model. Dashed lines show a simple power-law model. The best-fit parameters of the models are shown on each plot.

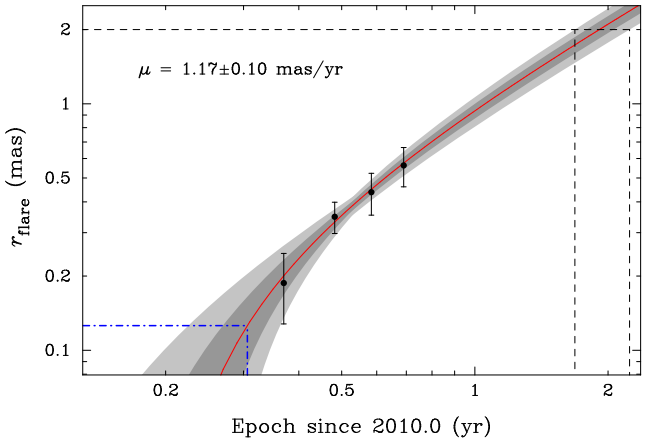

Figure 10. Flare propagation down the jet. The measurements denote distances from the jet origin to the VLBI core at the frequency of maximum emission (Fig. 9, top) at the four observing VLBA epochs. The solid line represents the best linear fit. Dark and light shaded areas show 1σ and 2σ confidence regions of the fit, respectively. Dot–dashed lines indicate the epoch 2010.31 of the γ-ray flare and the corresponding distance 0.12 mas of the γ-ray emission zone from the central engine. Dashed lines indicate the expected epoch range (2012) when the flare reaches the jet component J2 at 2-mas separation from the true jet base, assuming a constant flare propagation speed.

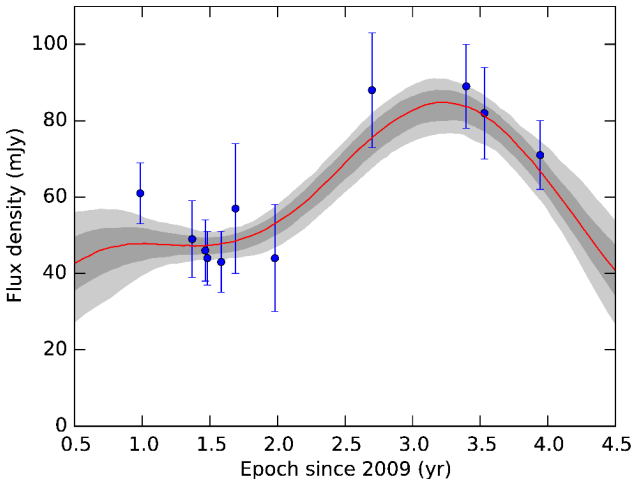

Figure 11. Flux density at 15 GHz of the jet component J2 located at 2 mas from the jet origin. The significant increase of the flux density in 2012 is probably a result of the flare that originated in 2010 and reached this jet region in 2012, as expected from the assumed constant flare propagation speed. Error bars represent 1σ uncertainties of individual measurements. The smooth solid curve shows the Gaussian process fit. Dark and light filled areas correspond to 68 per cent and 95 per cent confidence intervals of the fit, respectively.

the $\beta_{app}^{max} = 21\,c$ detected in the high-redshift ($z = 1.07$) BL Lac object 1514 + 197 (Lister et al. 2016). Similarly, by analysing multifrequency time delays of the flares and measuring the core shifts in the blazars 3C 454.3 (Kutkin et al. 2014) and 0235 + 164 (Kutkin et al. 2018) it was found that this approach yields the source jet speed, which is by a factor of a few higher than the estimates based on kinematic analysis.

Now, we assume that the jet of PKS 2233 − 148 in the core region is in equipartition between the particle and magnetic field energy density ($k_r = 1$), has a spectral index −0.5, and is viewed at the critical angle $\theta \simeq \Gamma^{-1}$. Then the magnetic field in gauss at 1 pc of actual distance from the jet apex can be estimated using the

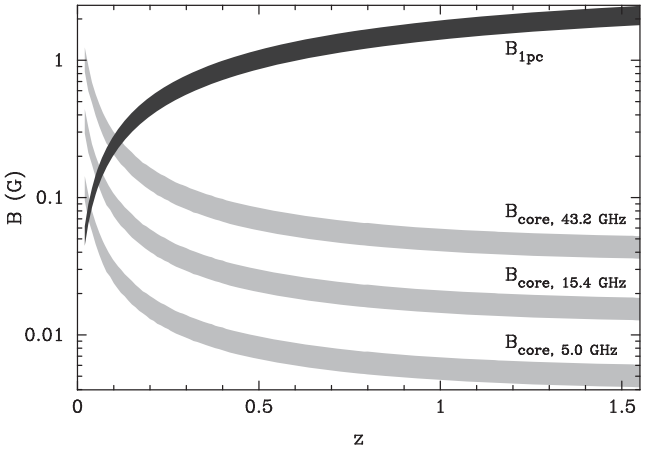

Figure 12. Magnetic field constraints obtained from the core-shift measurements and the flare propagation speed. The dark grey area shows estimates of the magnetic field at 1-pc distance from the jet origin, while the light grey stripes represent the magnetic field at the core at 43.2, 15.4 and 5.0 GHz.

following relationship (Pushkarev et al. 2012):

$$B_1 \simeq 0.04\,\Omega_{r\nu}^{3/4}\,(1+z)^{1/2}(1+\beta_{\rm app}^2)^{1/8}\,, \quad (5)$$

where $\Omega_{r\nu}$ is the core-shift measure defined in Lobanov (1998) as

$$\Omega_{r\nu} = 4.85\times10^{-9}\,\frac{\Delta r_{{\rm core},\,\nu_1\nu_2}\,D_L}{(1+z)^2}\,\frac{\nu_1\nu_2}{\nu_2-\nu_1}\ {\rm pc\,GHz}, \quad (6)$$

where $\Delta r_{{\rm core},\,\nu_1\nu_2}$ is the core shift in mas, D_L is the luminosity distance in pc, and $\beta_{\rm app} = 1.58\times10^{-8} D_L\mu/(1+z)$. The magnetic field strength at the apparent VLBI core at a given frequency can be calculated as $B_{\rm core} = B_1 r_{\rm core}^{-1}$, where the absolute distance in parsecs of the core from the true jet base $r_{\rm core}$ is given by (Lobanov 1998)

$$r_{\rm core}(\nu) = \frac{\Omega_{r\nu}}{\nu\,\sin\theta} \approx \frac{\Omega_{r\nu}(1+\beta_{\rm app}^2)^{1/2}}{\nu}, \quad (7)$$

where ν is the observed frequency in GHz.

In Fig. 12, we plot the derived B_1 and $B_{\rm core}$ for the 43-, 15- and 5-GHz cores as functions of redshift. Assuming that $z > 0.5$, the magnetic field at a distance of 1 pc from the central engine is of the order of 1 G. We note that the estimates of $B_{\rm core}$ at 15 GHz derived from the core-shift analysis are comparable (lower by a factor of a few) to those inferred from the synchrotron spectrum fits (Section 3.7), if the source Doppler factor is moderate ($\delta \lesssim 5$), as is often observed to be the case in BL Lacertae objects (Hovatta et al. 2009; Liodakis et al. 2017).

3.9 Location of the γ-ray emission region and the source of seed photons

In order to estimate the location of the γ-ray emission zone in PKS 2233 − 148 we extrapolated the $r_{\rm flare}$ dependence (Fig. 10) back to the epoch of the γ-ray flare, 2010.31 (Fig. 2). This yields an angular separation of 0.12 ± 0.03 mas from the true jet base, which corresponds to the VLBI core position at 24 GHz (Fig. 6). On a linear scale,this separation is >0.7 ± 0.2 pc in projection, which exceeds a de-projected separation of 8 ± 2 pc if we assume a jet viewing angle of 5°. Considering the second peak of the γ-ray data at epoch 2010.46 (2010 June 17), we inferred a distance of about 0.3 mas from the jet apex. This distancecorresponds to the innermost jet feature J4 detected at 24 and 43 GHz, setting an absolute distance of about 20 pc for another possible location

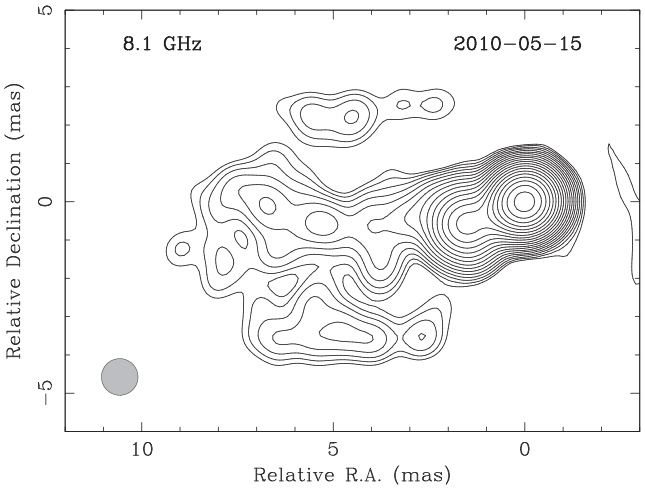

Figure 13. Total-intensity map of PKS 2233−148 at 8.1 GHz at the epoch 2010-05-15 from Fig. 1 but convolved with a circular beam of the size of the minor axis of the original image. Emission at the jet edges indicates the presence of a distinct boundary layer.

of the γ-ray emission site. These assessments favour a scenario in which the γ-ray production zone is located at large distances from a central energy generator (beyond the broad-line region or torus) and is probably associated with one or more standing shocks in a relativistic outflow of PKS 2233 − 148, as suggested by the complex structure of the major high-energy flares in the source. A similar conclusion regarding the remotness of the γ-ray emission region in blazars on scales of parsecs from the central black hole was also reached from other arguments in a number of recent single-source studies of 1510 − 089 (Marscher et al. 2010), OJ 287 (Agudo et al. 2011), 3C 345 (Schinzel et al. 2012), CTA 102 (Casadio et al. 2015), 1502 + 106 (Karamanavis et al. 2016), BL Lacertae (Wehrle et al. 2016), and also from statistical results from the F-GAMMA project (Fuhrmann et al. 2016). At the same time, the arguments based on short-scale variability and breaks in GeV spectra discussed in the Introduction indicate that the high-energy production site is in the immediate vicinity of the black hole.

Another noticeable feature of the parsec-scale morphology of the source is the presence of a sheath around the jet, as indicated in the 8- and 15-GHz maps (Fig. 1), which provide a combination of a high angular resolution and sensitivity. In order to better visualize the sheath emission we convolved the 8.1-GHz image at the epoch 2010-05-15 with a circular beam, setting its FWHM to that of the minor axis of the original map (Fig. 13). The fact that this sheath is slower than the central spine might mean that it acts as a source of additional seed photons for the γ-ray radiation (e.g. Marscher et al. 2010; Aleksić et al. 2014). Thus, the high-energy emission of the source can be formed through (i) the synchrotron self-Compton mechanism acting in its relativistic outflow and the upscattering of low-energy synchrotron seed photons; and (ii) external Compton scattering resulting from a photon field in the sheath.

While detailed modelling of the spectral energy distribution (SED) is beyond the scope of this paper, based on the publicly available non-simultaneous data in the SSDC SED builder tool[5] it seems that, when the source is in a high state in γ-rays, the luminosity of the inverse Compton peak is higher than that of the synchrotron peak, indicating that an additional external photon field

[5]https://tools.ssdc.asi.it

is indeed needed. However, this should be verified with simultaneous data in all bands, taken at both low and high activity states of the source.

We can also speculate that if instead of the epoch of the γ-ray peak we consider the epoch at which the flare starts rising (a few weeks before the peak), then the γ-ray emission site could be in the immediate vicinity of the central machine. This scenario is vulnerable, however, as a plasma cloud moving fast down the jet leaves the seed photon area rapidly, while the flare is still reaching its maximum.

4 SUMMARY

We performed a radio and γ-ray joint study of the BL Lacertae object PKS 2233 − 148, using multiwavelength data in the period 2009–2012. The VLBA observations at 4.6–43.2 GHz reveal the core-dominated, one-sided and relatively straight jet morphology of the source extending up to 8 mas at a position angle of 112°. By analysing jet widths derived from the structure model fits we established that the outflow has a conical shape. This sets a lower limit of about 0.1 on the source unknown redshift.

We measured the frequency-dependent shift vectors of the apparent core position using a method based on results from (i) structure model fitting and (ii) image alignment achieved by implementing a 2D cross-correlation technique on the optically thin jet regions. The magnitude of the core shifts ranges from 0.04 to 0.7 mas, with a typical uncertainty of 45 μas. The directions of the shift vectors are predominantly aligned with the median jet position angle, deviating from it by $\lesssim 10^{\circ}$ in 68 per cent of cases. The derived core shifts show a frequency dependence $\propto \nu^{-1/k_{\rm r}}$, with $k_r \approx 1$ indicating that nuclear opacity is dominated by synchrotron self-absorption, and that the physical conditions in the jet on scales probed by the VLBA observations are close to equipartition. We did not find evidence for significant changes in $k_{\rm r}$ between the observing epochs covering a time-scale of four months, during which a flare was developing down the jet. This suggests that the transverse size of the disturbance area is significantly smaller than the jet part constrained by the magnitude of the core-shift effect within a frequency range of 5–43 GHz. The VLBI core position $r_{\rm core}$ as a function of wavelength follows an $r_{\rm mas}^{\rm core} \approx 0.1\lambda_{\rm cm}$ dependence. The magnetic field at a distance of 1 pc from the jet apex derived from the core shift measurements is about 1 G.

We have presented a method of independent assessment of jet kinematics based on core-shift measurements and the evolution of the synchrotron spectrum of the VLBI core. The turnover frequency of the core spectrum linearly shifts towards lower frequencies with time, as the flare originating in 2010 April in γ-rays propagates down the jet. The speed of this propagation is about 1.2 mas yr^{-1} and probably represents the bulk flow speed. It is much higher than results from traditional kinematics based on tracking bright jet features, namely 0.045 mas yr^{-1} (Lister et al. 2016).

We have found indications that the γ-ray production zone in the source is located at large distances, 10–20 pc, from a central engine, and can be associated with the stationary radio-emitting jet features observed with VLBI. This favours synchrotron self-Compton scattering as the dominant high-energy radiation mechanism in the relativistic jet of the source. Direct observational evidence for a boundary layer around the jet suggests that the sheath might be an additional source of seed photons for external Compton scattering acting in the source.

ACKNOWLEDGEMENTS

We would like to thank the anonymous referee as well as E. Ros for useful comments and suggestions. The VLBA data processing and core-shift analysis were supported by the Russian Science Foundation grant 16-12-10481. The radio/γ-ray joint analysis was supported by the Academy of Finland projects 296010 and 318431. TH acknowledges support from the Turku Collegium of Science and Medicine. This research has made use of data from the MOJAVE data base, which is maintained by the MOJAVE team (Lister et al. 2018). The MOJAVE project was supported by NASA-*Fermi* GI grants NNX08AV67G, NNX12A087G and NNX15AU76G. This work made use of the Swinburne University of Technology software correlator (Deller et al. 2011), developed as part of the Australian Major National Research Facilities Programme and operated under licence. This research has made use of data from the OVRO 40-m monitoring program (Richards et al. 2011), which is supported in part by NASA grants NNX08AW31G, NNX11A043G and NNX14AQ89G and NSF grants AST-0808050 and AST-1109911. The National Radio Astronomy Observatory is a facility of the National Science Foundation operated under cooperative agreement by Associated Universities, Inc.

REFERENCES

Abdo A. A. et al., 2011, ApJ, 730, 101
Acero F. et al., 2015, ApJS, 218, 23
Agudo I. et al., 2011, ApJ, 726, L13
Aleksić J. et al., 2014, A&A, 569, A46
Alexander T., 1997, in Maoz D., Sternberg A., Leibowitz E. M., eds, Astrophysics and Space Science Library Vol. 218, Astronomical Time Series. Kluwer, Dordrecht, p. 163
Asada K., Nakamura M., 2012, ApJ, 745, L28
Atwood W. B. et al., 2009, ApJ, 697, 1071
Bai J. M., Liu H. T., Ma L., 2009, ApJ, 699, 2002
Blandford R. D., 1990, in Blandford R. D., Netzer H., Woltjer L., Courvoisier T. J.-L., Mayor M., eds, Active Galactic Nuclei. Springer-Verlag, Berlin Heidelberg, p. 161
Blandford R. D., Königl A., 1979, ApJ, 232, 34
Casadio C. et al., 2015, ApJ, 813, 51
Cohen M. H. et al., 2014, ApJ, 787, 151
Cornwell T. J., Wilkinson P. N., 1981, MNRAS, 196, 1067
Deller A. T. et al., 2011, PASP, 123, 275
Drinkwater M. J. et al., 1997, MNRAS, 284, 85
Fromm C. M., 2015, Astron. Nach., 336, 447
Fromm C. M. et al., 2010, in Savolainen T., Ros E., Porcas R.W., Zensus J.A., eds, Proceedings of the meeting 'Fermi meets Jansky - AGN at Radio and Gamma-Rays'. Max-Planck-Insitute fuer Radioastronomie, Bonn, p. 97
Fuentes A., Gómez J. L., Martí J. M., Perucho M., 2018, ApJ, 860, 121
Fuhrmann L. et al., 2016, A&A, 596, A45
Gould R. J., 1979, A&A, 76, 306
Greisen E. W., 2003, in Heck A., ed., Astrophysics and Space Science Library 285, Information Handling in Astronomy – Historical Vistas. Kluwer, Dordrecht, p. 109
Hada K., Doi A., Kino M., Nagai H., Hagiwara Y., Kawaguchi N., 2011, Nature, 477, 185
Hovatta T., Lister M. L., Aller M. F., Aller H. D., Homan D. C., Kovalev Y. Y., Pushkarev A. B., Savolainen T., 2012, AJ, 144, 105
Hovatta T., Valtaoja E., Tornikoski M., Lähteenmäki A., 2009, A&A, 498, 723
Hovatta T. et al., 2014, AJ, 147, 143
Högbom J. A., 1974, A&AS, 15, 417
Jennison R. C., 1958, MNRAS, 118, 276
Kadler M., Ros E., Lobanov A. P., Falcke H., Zensus J. A., 2004, A&A, 426, 481

Karamanavis V. et al., 2016, A&A, 590, A48
Kardashev N. S., 1962, Soviet Astron., 6, 317
Komatsu E. et al., 2009, ApJS, 180, 330
Konigl A., 1981, ApJ, 243, 700
Kovalev Y. Y. et al., 2005, AJ, 130, 2473
Kovalev Y. Y. et al., 2009, ApJ, 696, L17
Kravchenko E. V., Kovalev Y. Y., Hovatta T., Ramakrishnan V., 2016, MNRAS, 462, 2747
Kutkin A. M. et al., 2014, MNRAS, 437, 3396
Kutkin A. M. et al., 2018, MNRAS, 475, 4994
Lewis J. P., 1995, Vision Interface, 120
Liodakis I. et al., 2017, MNRAS, 466, 4625
Lisakov M. M., Kovalev Y. Y., Savolainen T., Hovatta T., Kutkin A. M., 2017, MNRAS, 468, 4478
Lister M. L., Aller M. F., Aller H. D., Hodge M. A., Homan D. C., Kovalev Y. Y., Pushkarev A. B., Savolainen T., 2018, ApJS, 234, 12
Lister M. L., Homan D. C., 2005, AJ, 130, 1389
Lister M. L. et al., 2016, AJ, 152, 12
Lobanov A. P., 1998, A&A, 330, 79
Marscher A. P., 1983, ApJ, 264, 296
Marscher A. P., 1987, in Superluminal radio sources. Cambridge University Press, Cambridge and New York, p. 280
Marscher A. P., Gear W. K., 1985, ApJ, 298, 114
Marscher A. P. et al., 2010, ApJ, 710, L126
Mattox J. R. et al., 1996, ApJ, 461, 396
Mizuno Y., Gómez J. L., Nishikawa K.-I., Meli A., Hardee P. E., Rezzolla L., 2015, ApJ, 809, 38
O'Sullivan S. P., Gabuzda D. C., 2009, MNRAS, 400, 26
Pacholczyk A. G., 1970, Radio Astrophysics. Nonthermal Processes in Galactic and Extragalactic Sources. Freeman, San Francisco
Plavin A. V., Kovalev Y. Y., Pushkarev A. B., Lobanov A. P., 2018, MNRAS, submitted (arXiv:1811.02544)
Poutanen J., Stern B., 2010, ApJ, 717, L118
Pushkarev A. B., Hovatta T., Kovalev Y. Y., Lister M. L., Lobanov A. P., Savolainen T., Zensus J. A., 2012, A&A, 545, A113
Pushkarev A. B., Kovalev Y. Y., 2012, A&A, 544, A34
Pushkarev A. B., Kovalev Y. Y., Lister M. L., 2010, ApJ, 722, L7
Pushkarev A. B., Kovalev Y. Y., Lister M. L., Savolainen T., 2017, MNRAS, 468, 4992
Readhead A. C. S., Walker R. C., Pearson T. J., Cohen M. H., 1980, Nature, 285, 137
Richards J. L. et al., 2011, ApJS, 194, 29
Sbarufatti B., Treves A., Falomo R., Heidt J., Kotilainen J., Scarpa R., 2006, AJ, 132, 1
Schinzel F. K., Lobanov A. P., Taylor G. B., Jorstad S. G., Marscher A. P., Zensus J. A., 2012, A&A, 537, A70
Schwab F. R., 1980, in Rhodes W. T., ed., Society of Photo-Optical Instrumentation Engineers (SPIE) Conference Series Vol. 231, Bellingham, WA, p. 18
Shepherd M. C., 1997, in Hunt G., Payne H. E., eds, Astronomical Society of the Pacific Conference Series Vol. 125, Astronomical Data Analysis Software and Systems VI. Astron. Soc. Pac., San Francisco, p. 77
Slish V. I., 1963, Nature, 199, 682
Sokolovsky K. V., Kovalev Y. Y., Pushkarev A. B., Lobanov A. P., 2011, A&A, 532, A38
Tavecchio F., Ghisellini G., Bonnoli G., Ghirlanda G., 2010, MNRAS, 405, L94
Twiss R. Q., Carter A. W. L., Little A. G., 1960, The Observatory, 80, 153
Türler M., Courvoisier T. J.-L., Paltani S., 1999, A&A, 349, 45
Voitsik P. A., Pushkarev A. B., Plavin A. V., Kovalev Y. Y., Lobanov A. P., Ipatov A. V., 2018, Astronomy Reports, in press, preprint (arXiv:1809.10011)
Wehrle A. E. et al., 2016, ApJ, 816, 53
Yan D., Wu Q., Fan X., Wang J., Zhang L., 2018, ApJ, 859, 168

APPENDIX A: MAGNETIC FIELD FROM SYNCHROTRON SELF-ABSORPTION

The interpretation of a radio spectrum with a low-frequency turnover caused by synchrotron self-absorption, and the determination of physical parameters within this assumption date back to the 1960s (see, for example, one of the pioneering works Slish 1963). In particular, the magnetic field associated with a source of synchrotron emission can be inferred. However, the approximate values of the numerical coefficient in the formula that are a function of a spectral index α ($S_\nu \propto \nu^\alpha$) of the optically thin part of a synchrotron spectrum are tabulated for a limited number of α values, ranging from -0.25 to -1.0 (Marscher 1983). The relation for this coefficient was previously discussed by Gould (1979). In this Appendix, we derive a formula for this coefficient that can be computed precisely.

Following Pacholczyk (1970), the intensity of emission in the case of synchrotron self-absorption is

$$S_\nu = F(\nu_1)\, J\left(\frac{\nu}{\nu_1}, s\right), \tag{A1}$$

where $s = 1 - 2\alpha$ is the power-law index of the energy distribution $N(E) = N_0 E^{-s}$ of emitting electrons, and

$$J\left(\frac{\nu}{\nu_1}, s\right) = \left(\frac{\nu}{\nu_1}\right)^{5/2} \left\{1 - \exp\left[-\left(\frac{\nu}{\nu_1}\right)^{-(s+4)/2}\right]\right\}, \tag{A2}$$

where ν_1 is the frequency at which the optical depth $\tau = 1$. The source function $F(\nu_1)$ for a spherical, uniform emitting region with observed angular size $\theta = 2R(1+z)^2/D$ at the luminosity distance D is

$$\begin{aligned} F(\nu_1) &= \frac{\left(\pi\theta^2 R/3\right)\varepsilon_{\nu_1}\left[\delta/(1+z)\right]^{2-\alpha}}{2\kappa_{\nu_1} R\left[\delta/(1+z)\right]^{(3-2\alpha)/2}} \\ &= \frac{\pi}{6}\theta^2 \frac{\varepsilon_{\nu_1}}{\kappa_{\nu_1}}\left(\frac{\delta}{1+z}\right)^{1/2}, \end{aligned} \tag{A3}$$

where

$$\varepsilon_{\nu_1} = c_5(s)\, N_0 B_\perp^{(s+1)/2}\left(\frac{\nu_1}{2c_1}\right)^{(1-s)/2} \tag{A4}$$

and

$$\kappa_{\nu_1} = c_6(s)\, N_0 B_\perp^{(s+2)/2}\left(\frac{\nu_1}{2c_1}\right)^{-(s+4)/2} \tag{A5}$$

are the emission and absorption coefficients, respectively, and $B_\perp$ is the component of the magnetic field perpendicular to the line of sight. Constants and functions are:

$$c_1 = \frac{3e}{4\pi m^3 c^5}, \qquad c_3 = \frac{\sqrt{3}e^3}{4\pi mc^2}, \tag{A6}$$

$$c_5 = \frac{1}{4} c_3 \frac{s+7/3}{s+1}\,\Gamma\left(\frac{3s-1}{12}\right)\Gamma\left(\frac{3s+7}{12}\right), \tag{A7}$$

$$c_6 = \frac{1}{32}\left(\frac{c}{c_1}\right)^2 c_3\left(s+\frac{10}{3}\right)\Gamma\left(\frac{3s+2}{12}\right)\Gamma\left(\frac{3s+10}{12}\right), \tag{A8}$$

where e and m are the charge and mass of an electron, respectively, c is the speed of light in vacuum, and Γ is the Euler gamma function.

Substituting equations (A2)–(A8) into (A1) we obtain

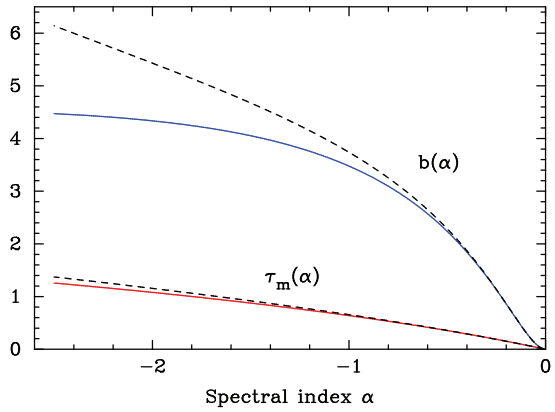

Figure A1. Coefficient $b(\alpha)$ and optical depth $\tau_{\rm m}(\alpha)$ as a function of the spectral index α. Dashed lines represent approximate solutions derived using equation (A12).

$$S_\nu = \frac{\pi}{6}\frac{c_5(s)}{c_6(s)}(2c_1)^{-5/2}\theta^2 B_\perp^{-1/2}\nu^{5/2}\left(\frac{\delta}{1+z}\right)^{1/2}\left[1-{\rm e}^{-\tau_\nu}\right], \quad \text{(A9)}$$

where $\tau_\nu = (\nu/\nu_1)^{-(s+4)/2}$. Then the flux density at the turnover frequency $\nu_{\rm m}$ extrapolated from the straight-line slope of the optically thin part of synchrotron spectrum is

$$\begin{aligned} S'_{\rm m} &= S_\nu|_{\nu=\nu_m}\,{\rm e}^{\tau_{\rm m}} \\ &= \left[\frac{\pi}{6}\frac{c_5(s)}{c_6(s)}(2c_1)^{-5/2}({\rm e}^{\tau_{\rm m}}-1)\right]\theta^2 B_\perp^{-1/2}\nu_{\rm m}^{5/2}\left(\frac{\delta}{1+z}\right)^{1/2}. \end{aligned} \quad \text{(A10)}$$

The optical depth $\tau_{\rm m}$ at $\nu_{\rm m}$ is found from the equation

$${\rm e}^{\tau_{\rm m}} = 1+\left(1-\frac{2\alpha}{5}\right)\tau_{\rm m}. \quad \text{(A11)}$$

By developing the exponential in equation (A11) to the third order, Türler, Courvoisier & Paltani (1999) obtained the approximate solution

$$\tau_{\rm m} = \frac{3}{2}\left(\sqrt{1-\frac{16\alpha}{15}}-1\right), \quad \text{(A12)}$$

which is accurate enough, deviating by less than 5 per cent from the exact numerical solution for $\alpha \gtrsim -1.55$ (Fig. A1).

Solving equation (A10) for the normal component of the magnetic field, we have

$$B_\perp = 10^{-5}\,b(s)\,\theta^4\,S'^{-2}_{\rm m}\,\nu^5_{\rm m}\left(\frac{\delta}{1+z}\right), \quad \text{(A13)}$$

where the source size θ is in mas, the flux density is in Jy, the turnover frequency ν_m is in GHz, the magnetic field is in G, and

$$b(s) = 5.5\times10^{62}\left[\frac{\pi}{6}\frac{c_5(s)}{c_6(s)}({\rm e}^{\tau_{\rm m}}-1)\right]^2(2c_1)^{-5}. \quad \text{(A14)}$$

In Fig. A1, we plot the coefficient b as a function of $\alpha = (1-s)/2$. The departure of the approximate solutions from the exact ones exceeds 5 per cent for $\alpha \lesssim -0.82$.

Table A1. Amplitude scale corrections for the S2087D VLBA experiment.

Antenna (1)	Band (2)	Epoch (3)	IF (4)	Correction (5)
BR	K	1	1–2	0.88
BR	K	1	3–4	0.85
BR	K	2,3,4	1–4	0.80
FD	U	1	1–4	1.09
FD	Q	1	1–4	1.15
KP	C	2,4	1–2	1.08
KP	X	1	1–2	0.90
KP	X	2,3,4	1–2	0.93
KP	K	All	1–4	1.10
LA	C	All	1–2	0.93
LA	K	All	1–4	0.90
OV	X	1	1–2	1.21
OV	X	3,4	1–2	1.17
SC	U	1	1–4	0.88
SC	Q	2	2,4	0.80

Column designation: (1) antenna name; (2) radio band name; (3) observation epoch (epochs are labelled as follows: 1 for 2010 May 15, 2 for 2010 June 25, 3 for 2010 August 1, 4 for 2010 September 9); (4) number of frequency channel (IF); (5) amplitude scale correction coefficient.

Table A2. Summary of image parameters. Columns are as follows: (1) epoch of observations, (2) central observing frequency, (3) *I* peak of image, (4) rms noise level of image, (5) thermal noise estimate, (6) bottom *I* contour level, (7) dynamic range of image, (8) total flux density from map, (9) full-width at half maximum (FWHM) major axis of restoring beam, (10) FWHM minor axis of restoring beam, (11) position angle of major axis of restoring beam.

Epoch	Freq. [GHz]	I_{peak} [mJy bm^{-1}]	I_{rms} [mJy bm^{-1}]	Thermal noise [mJy bm^{-1}]	I_{base} [mJy bm^{-1}]	DR	S_{VLBA} [mJy]	B_{maj} [mas]	B_{min} [mas]	B_{PA} [°]
(1)	(2)	(3)	(4)	(5)	(6)	(7)	(8)	(9)	(10)	(11)
2010-05-15	4.608	335	0.19	0.11	0.76	1756	505	4.40	1.74	− 2.0
2010-06-25	4.608	408	0.15	0.11	0.61	2676	569	4.97	1.87	− 7.6
2010-08-01	4.608	382	0.17	0.11	0.68	2235	538	4.54	1.80	− 3.5
2010-09-09	4.608	357	0.21	0.11	0.83	1723	510	4.50	1.79	− 2.0
2010-05-15	5.003	350	0.18	0.15	0.71	1979	519	4.14	1.65	− 3.3
2010-06-25	5.003	413	0.15	0.15	0.60	2737	570	4.74	1.76	− 8.1
2010-08-01	5.003	371	0.30	0.15	1.19	1243	542	3.51	1.39	− 2.2
2010-09-09	5.003	359	0.17	0.15	0.68	2115	514	4.21	1.67	− 2.2
2010-05-15	8.108	438	0.15	0.16	0.59	2963	588	2.35	0.95	− 0.7
2010-06-25	8.108	470	0.18	0.16	0.70	2677	615	2.71	1.03	− 5.9
2010-08-01	8.108	417	0.17	0.16	0.69	2410	566	2.46	0.97	− 1.7
2010-09-09	8.108	335	0.15	0.16	0.61	2203	478	2.49	0.99	− 1.8
2010-05-15	8.429	445	0.16	0.16	0.64	2778	595	2.31	0.92	− 2.2
2010-06-25	8.429	477	0.14	0.16	0.56	3429	624	2.68	0.99	− 7.5
2010-08-01	8.429	425	0.16	0.16	0.63	2707	569	2.44	0.95	− 3.1
2010-09-09	8.429	345	0.14	0.16	0.58	2396	487	2.45	0.96	− 3.1
2010-05-15	15.365	557	0.20	0.18	0.68	2853	697	1.58	0.49	− 11.9
2010-06-25	15.365	517	0.19	0.18	0.66	2735	648	1.57	0.51	− 10.2
2010-08-01	15.365	406	0.19	0.18	0.65	2179	545	1.37	0.48	− 6.6
2010-09-09	15.365	296	0.19	0.18	0.68	1523	426	1.38	0.48	− 6.4
2010-05-15	23.804	557	0.26	0.21	1.02	2181	685	0.96	0.29	− 12.3
2010-06-25	23.804	496	0.33	0.21	1.30	1521	616	1.12	0.29	− 15.4
2010-08-01	23.804	320	0.27	0.21	1.10	1167	449	0.95	0.27	− 12.6
2010-09-09	23.804	250	0.26	0.21	1.06	945	350	1.19	0.31	− 15.2
2010-05-15	43.217	511	0.40	0.32	1.41	1271	631	0.49	0.17	− 8.5
2010-06-25	43.217	450	0.44	0.32	1.55	1013	583	0.75	0.19	− 16.9
2010-08-01	43.217	442	0.92	0.45	3.23	479	585	0.97	0.19	− 16.3
2010-09-09	43.217	346	0.96	0.45	3.36	361	439	0.68	0.17	− 14.3

Table A3. Source models. Columns are as follows: (1) observation date, (2) name of the component, (3) flux density of the fitted Gaussian component, (4) position offset from the core component, (5) position angle of the component with respect to the core component, (6) full-width at half maximum major axis of the fitted Gaussian, (7) signal-to-noise ratio of the fitted Gaussian.

Date	Comp.	Flux density [Jy]	Distance [mas]	P.A. [°]	Size [mas]	SNR
(1)	(2)	(3)	(4)	(5)	(6)	(7)
			4.6 GHz			
2010-05-15	Core	0.304 ± 0.019	0.000	...	0.322 ± 0.014	535
	J2	0.127 ± 0.012	1.454 ± 0.036	113.7 ± 1.4	1.009 ± 0.070	207
	J1	0.068 ± 0.015	5.049 ± 0.515	100.5 ± 5.8	4.884 ± 1.030	23
2010-06-25	Core	0.363 ± 0.025	0.000	...	0.333 ± 0.016	428
	J2	0.127 ± 0.015	1.408 ± 0.048	114.2 ± 1.9	1.092 ± 0.094	134
	J1	0.068 ± 0.016	5.012 ± 0.557	103.0 ± 6.3	4.926 ± 1.114	20
2010-08-01	Core	0.350 ± 0.020	0.000	...	0.356 ± 0.014	618
	J2	0.115 ± 0.011	1.394 ± 0.040	112.0 ± 1.6	1.039 ± 0.078	180
	J1	0.065 ± 0.013	4.997 ± 0.461	102.1 ± 5.3	4.706 ± 0.922	27
2010-09-09	Core	0.327 ± 0.026	0.000	...	0.391 ± 0.022	315
	J2	0.109 ± 0.014	1.333 ± 0.051	115.2 ± 2.1	1.026 ± 0.100	104
	J1	0.066 ± 0.014	4.939 ± 0.479	101.6 ± 5.5	4.722 ± 0.958	25
			5.0 GHz			
2010-05-15	Core	0.329 ± 0.020	0.000	...	0.329 ± 0.014	547
	J2	0.117 ± 0.012	1.485 ± 0.038	113.4 ± 1.4	0.951 ± 0.074	166
	J1	0.067 ± 0.016	5.057 ± 0.572	101.9 ± 6.5	4.918 ± 1.144	19
2010-06-25	Core	0.382 ± 0.027	0.000	...	0.326 ± 0.016	387

Table A3 – *continued*

Date	Comp.	Flux density [Jy]	Distance [mas]	P.A. [°]	Size [mas]	SNR
(1)	(2)	(3)	(4)	(5)	(6)	(7)
	J2	0.114 ± 0.014	1.425 ± 0.046	112.4 ± 1.8	0.997 ± 0.090	125
	J1	0.067 ± 0.014	4.967 ± 0.508	102.7 ± 5.8	5.053 ± 1.016	26
2010-08-01	Core	0.360 ± 0.021	0.000	...	0.349 ± 0.014	560
	J2	0.117 ± 0.012	1.376 ± 0.043	113.3 ± 1.7	1.113 ± 0.084	173
	J1	0.059 ± 0.014	5.088 ± 0.499	103.1 ± 5.6	4.484 ± 0.998	21
2010-09-09	Core	0.331 ± 0.021	0.000	...	0.382 ± 0.018	474
	J2	0.115 ± 0.013	1.295 ± 0.047	115.3 ± 2.0	1.107 ± 0.092	145
	J1	0.060 ± 0.013	5.033 ± 0.452	101.2 ± 5.1	4.413 ± 0.904	25
			8.1 GHz			
2010-05-15	Core	0.449 ± 0.032	0.000	...	0.250 ± 0.012	376
	J2	0.098 ± 0.016	1.491 ± 0.073	112.4 ± 2.8	1.096 ± 0.146	57
	J1	0.044 ± 0.019	5.387 ± 0.931	101.0 ± 9.8	4.357 ± 1.862	6
2010-06-25	Core	0.469 ± 0.031	0.000	...	0.246 ± 0.012	438
	J2	0.106 ± 0.015	1.374 ± 0.076	113.0 ± 3.2	1.269 ± 0.152	72
	J1	0.043 ± 0.017	5.323 ± 0.871	102.0 ± 9.3	4.383 ± 1.742	7
2010-08-01	Core	0.420 ± 0.030	0.000	...	0.269 ± 0.014	393
	J2	0.103 ± 0.016	1.303 ± 0.087	113.2 ± 3.8	1.313 ± 0.174	58
	J1	0.045 ± 0.018	5.244 ± 0.893	101.3 ± 9.7	4.421 ± 1.786	7
2010-09-09	Core	0.335 ± 0.023	0.000	...	0.311 ± 0.016	397
	J2	0.101 ± 0.014	1.216 ± 0.076	114.8 ± 3.6	1.284 ± 0.152	72
	J1	0.043 ± 0.017	5.199 ± 0.916	101.5 ± 10.0	4.500 ± 1.832	7
			8.4 GHz			
2010-05-15	Core	0.455 ± 0.034	0.000	...	0.233 ± 0.012	359
	J2	0.098 ± 0.017	1.495 ± 0.082	112.7 ± 3.1	1.137 ± 0.164	50
	J1	0.044 ± 0.021	5.352 ± 1.036	103.6 ± 11.0	4.382 ± 2.072	5
2010-06-25	Core	0.480 ± 0.030	0.000	...	0.236 ± 0.010	508
	J2	0.099 ± 0.015	1.410 ± 0.074	112.8 ± 3.0	1.217 ± 0.148	69
	J1	0.044 ± 0.017	5.318 ± 0.830	103.1 ± 8.9	4.350 ± 1.660	8
2010-08-01	Core	0.429 ± 0.030	0.000	...	0.255 ± 0.012	411
	J2	0.100 ± 0.015	1.313 ± 0.085	112.6 ± 3.7	1.304 ± 0.170	59
	J1	0.043 ± 0.017	5.261 ± 0.853	102.6 ± 9.2	4.453 ± 1.706	8
2010-09-09	Core	0.343 ± 0.026	0.000	...	0.289 ± 0.016	336
	J2	0.102 ± 0.015	1.187 ± 0.080	114.3 ± 3.9	1.291 ± 0.160	66
	J1	0.045 ± 0.018	5.144 ± 0.878	102.7 ± 9.7	4.551 ± 1.756	8
			15.4 GHz			
2009-12-26	Core	0.383 ± 0.021	0.000	...	0.120 ± 0.004	680
	J3	0.051 ± 0.008	0.421 ± 0.029	114.6 ± 3.9	0.447 ± 0.058	59
	J2	0.061 ± 0.008	1.715 ± 0.021	111.0 ± 0.7	0.430 ± 0.042	102
	J1	0.030 ± 0.018	5.341 ± 1.434	101.5 ± 15.0	4.726 ± 2.868	4
2010-05-15	Core	0.584 ± 0.039	0.000	...	0.156 ± 0.008	448
	J3	0.037 ± 0.010	0.619 ± 0.035	115.0 ± 3.2	0.334 ± 0.070	24
	J2	0.049 ± 0.010	1.740 ± 0.043	111.2 ± 1.4	0.530 ± 0.086	40
	J1	0.031 ± 0.024	5.299 ± 1.679	98.0 ± 17.6	4.379 ± 3.358	2
2010-06-19	Core	0.577 ± 0.027	0.000	...	0.130 ± 0.006	922
	J3	0.059 ± 0.009	0.520 ± 0.034	119.2 ± 3.7	0.358 ± 0.068	86
	J2	0.046 ± 0.007	1.719 ± 0.037	111.3 ± 1.2	0.625 ± 0.074	79
	J1	0.034 ± 0.017	5.218 ± 1.150	100.3 ± 12.4	4.714 ± 2.300	5
2010-06-25	Core	0.534 ± 0.029	0.000	...	0.154 ± 0.006	650
	J3	0.045 ± 0.009	0.589 ± 0.028	118.4 ± 2.7	0.377 ± 0.056	46
	J2	0.044 ± 0.007	1.727 ± 0.042	110.8 ± 1.4	0.615 ± 0.084	55
	J1	0.029 ± 0.021	5.411 ± 1.624	102.0 ± 16.7	4.606 ± 3.248	3
2010-08-01	Core	0.439 ± 0.031	0.000	...	0.200 ± 0.010	380
	J3	0.041 ± 0.010	0.641 ± 0.032	118.4 ± 2.9	0.358 ± 0.064	32
	J2	0.043 ± 0.008	1.716 ± 0.057	112.9 ± 1.9	0.705 ± 0.114	40
	J1	0.027 ± 0.020	5.335 ± 1.530	100.1 ± 16.0	4.187 ± 3.060	3
2010-09-09	Core	0.298 ± 0.025	0.000	...	0.190 ± 0.012	274
	J3	0.055 ± 0.012	0.348 ± 0.035	100.4 ± 5.6	0.404 ± 0.068	37

Table A3 – *continued*

Date	Comp.	Flux density [Jy]	Distance [mas]	P.A. [°]	Size [mas]	SNR
(1)	(2)	(3)	(4)	(5)	(6)	(7)
	J2	0.057 ± 0.017	1.474 ± 0.164	110.6 ± 6.3	1.198 ± 0.328	14
	J1	0.022 ± 0.017	5.771 ± 1.463	99.1 ± 14.2	3.910 ± 2.926	2
2010-12-24	Core	0.306 ± 0.019	0.000	...	0.000 ± 0.010	526
	J3	0.060 ± 0.009	0.442 ± 0.031	98.9 ± 4.0	0.171 ± 0.062	88
	J2	0.046 ± 0.009	1.411 ± 0.077	110.5 ± 3.1	0.790 ± 0.154	36
	J1	0.023 ± 0.022	4.943 ± 2.275	95.5 ± 24.7	4.094 ± 4.550	2
2011-09-12	Core	0.644 ± 0.039	0.000	...	0.000 ± 0.008	559
	J3	0.071 ± 0.014	0.269 ± 0.073	103.3 ± 15.2	0.756 ± 0.146	32
	J2	0.088 ± 0.015	1.611 ± 0.044	110.7 ± 1.6	0.494 ± 0.088	54
	J1	0.029 ± 0.032	5.275 ± 2.814	101.1 ± 28.1	4.401 ± 5.628	1
2012-05-24	Core	1.029 ± 0.034	0.000	...	0.090 ± 0.002	1785
	J3	0.053 ± 0.008	0.506 ± 0.032	94.3 ± 3.6	0.286 ± 0.064	79
	J2	0.089 ± 0.011	1.612 ± 0.031	113.0 ± 1.1	0.609 ± 0.062	100
	J1	0.027 ± 0.016	5.417 ± 1.109	101.0 ± 11.6	3.927 ± 2.218	4
2012-07-12	Core	0.716 ± 0.028	0.000	...	0.140 ± 0.004	1273
	J3	0.066 ± 0.009	0.538 ± 0.026	98.9 ± 2.8	0.328 ± 0.052	94
	J2	0.082 ± 0.012	1.561 ± 0.034	114.0 ± 1.2	0.585 ± 0.068	74
	J1	0.040 ± 0.032	4.142 ± 2.124	97.8 ± 27.1	5.239 ± 4.248	2
2012-12-10	Core	0.857 ± 0.027	0.000	...	0.062 ± 0.002	1970
	J3	0.049 ± 0.006	0.644 ± 0.027	98.6 ± 2.4	0.447 ± 0.054	96
	J2	0.071 ± 0.009	1.569 ± 0.027	113.0 ± 1.0	0.534 ± 0.054	99
	J1	0.035 ± 0.020	4.964 ± 1.369	101.0 ± 15.4	4.717 ± 2.738	4
2016-09-17	Core	0.470 ± 0.031	0.000	...	0.061 ± 0.010	472
	J3	0.103 ± 0.016	0.401 ± 0.036	105.2 ± 5.1	0.347 ± 0.072	72
	J2	0.072 ± 0.016	1.695 ± 0.091	109.0 ± 3.1	0.838 ± 0.182	29
	J1	0.030 ± 0.021	5.485 ± 1.554	105.8 ± 15.8	4.362 ± 3.108	3
			23.8 GHz			
2010-05-15	Core	0.498 ± 0.026	0.000	...	0.044 ± 0.002	754
	J4	0.112 ± 0.012	0.147 ± 0.003	92.9 ± 1.2	0.000 ± 0.006	165
	J3	0.026 ± 0.006	0.600 ± 0.039	114.5 ± 3.7	0.389 ± 0.078	26
	J2	0.033 ± 0.007	1.756 ± 0.052	109.9 ± 1.7	0.542 ± 0.104	28
2010-06-25	Core	0.436 ± 0.032	0.000	...	0.009 ± 0.002	376
	J4	0.109 ± 0.017	0.164 ± 0.006	101.2 ± 2.1	0.000 ± 0.012	86
	J3	0.027 ± 0.008	0.661 ± 0.038	116.4 ± 3.3	0.320 ± 0.076	19
	J2	0.031 ± 0.009	1.744 ± 0.081	110.0 ± 2.7	0.652 ± 0.162	17
2010-08-01	Core	0.246 ± 0.022	0.000	...	0.013 ± 0.004	258
	J4	0.140 ± 0.017	0.163 ± 0.006	104.4 ± 2.1	0.131 ± 0.012	135
	J3	0.019 ± 0.005	0.788 ± 0.024	123.0 ± 1.7	0.228 ± 0.048	23
		0.007 ± 0.003	1.389 ± 0.042	116.5 ± 1.7	0.200 ± 0.084	11
	J2	0.019 ± 0.004	1.858 ± 0.041	112.6 ± 1.3	0.420 ± 0.082	27
2010-09-09	Core	0.185 ± 0.023	0.000	...	0.027 ± 0.008	135
	J4	0.111 ± 0.018	0.175 ± 0.012	107.6 ± 3.6	0.192 ± 0.022	75
	J3	0.021 ± 0.007	0.763 ± 0.031	118.3 ± 2.3	0.257 ± 0.062	19
		0.008 ± 0.003	1.330 ± 0.040	113.2 ± 1.7	0.200 ± 0.080	15
	J2	0.017 ± 0.005	1.844 ± 0.062	111.5 ± 1.9	0.511 ± 0.124	18
			43.2 GHz			
2010-05-15	Core	0.487 ± 0.025	0.000	...	0.026 ± 0.000	740
	J4	0.112 ± 0.014	0.129 ± 0.005	91.4 ± 2.2	0.100 ± 0.010	124
	J3	0.015 ± 0.005	0.667 ± 0.062	120.0 ± 5.3	0.379 ± 0.124	10
	J2	0.019 ± 0.007	1.806 ± 0.111	105.3 ± 3.5	0.606 ± 0.222	8
2010-06-25	Core	0.412 ± 0.025	0.000	...	0.028 ± 0.002	559
	J4	0.133 ± 0.014	0.134 ± 0.006	87.9 ± 2.6	0.145 ± 0.012	156
	J2	0.019 ± 0.007	1.813 ± 0.097	110.8 ± 3.1	0.595 ± 0.194	10
	J3	0.018 ± 0.005	0.686 ± 0.029	116.3 ± 2.4	0.247 ± 0.058	20
2010-08-01	Core	0.444 ± 0.030	0.000	...	0.051 ± 0.002	431
	J4	0.103 ± 0.016	0.183 ± 0.005	94.9 ± 1.6	0.005 ± 0.010	88
	J3	0.022 ± 0.008	0.761 ± 0.035	95.5 ± 2.6	0.225 ± 0.070	14

Table A3 – *continued*

Date	Comp.	Flux density [Jy]	Distance [mas]	P.A. [°]	Size [mas]	SNR
(1)	(2)	(3)	(4)	(5)	(6)	(7)
	J2	0.018 ± 0.006	1.980 ± 0.030	115.7 ± 0.9	0.238 ± 0.060	17
2010-09-09	Core	0.241 ± 0.019	0.000	...	0.011 ± 0.002	309
	J4	0.067 ± 0.010	0.197 ± 0.011	104.7 ± 3.2	0.190 ± 0.022	77
	J3	0.014 ± 0.005	0.840 ± 0.020	118.3 ± 1.4	0.128 ± 0.040	18
	J2	0.013 ± 0.005	1.765 ± 0.030	107.1 ± 1.0	0.153 ± 0.060	12

Table A4. Image shift, core-offset shift, and core-shift vectors measured for the frequency pairs ν_1 and ν_2.

Epoch	ν_1 ν_2 [GHz]	Δr_{12} [mas]	$r_1 - r_2$ [mas]	$\Delta r_{\mathrm{core},\nu_1\nu_2}$ [mas]	P.A.$_{\Delta r_{12}}$ [°]	P.A.$_{r_1-r_2}$ [°]	P.A.$_{\Delta r_{\mathrm{core},\nu_1\nu_2}}$ [°]	$\lambda_2 - \lambda_1$ [cm]
(1)	(2)	(3)	(4)	(5)	(6)	(7)	(8)	(9)
2010-05-15	43.2 4.6	0.794	0.189	0.615	101	117	96	5.816
2010-05-15	43.2 5.0	0.671	0.139	0.539	100	117	96	5.302
2010-05-15	43.2 8.1	0.242	0.010	0.244	97	− 159	95	3.006
2010-05-15	43.2 8.4	0.285	0.014	0.278	108	171	106	2.865
2010-05-15	43.2 15.4	0.090	0.013	0.088	90	168	82	1.258
2010-05-15	43.2 23.8	0.030	0.012	0.037	90	− 152	73	0.566
2010-05-15	23.8 4.6	0.713	0.189	0.527	105	113	102	5.250
2010-05-15	23.8 5.0	0.626	0.140	0.487	107	112	105	4.736
2010-05-15	23.8 8.1	0.190	0.003	0.188	108	53	109	2.440
2010-05-15	23.8 8.4	0.228	0.009	0.220	113	111	113	2.299
2010-05-15	23.8 15.4	0.085	0.009	0.078	135	102	138	0.692
2010-05-15	15.4 4.6	0.560	0.181	0.382	106	114	102	4.558
2010-05-15	15.4 5.0	0.532	0.131	0.401	106	112	104	4.044
2010-05-15	15.4 8.1	0.153	0.007	0.160	101	− 59	102	1.748
2010-05-15	15.4 8.4	0.153	0.001	0.153	101	− 161	101	1.607
2010-05-15	8.4 4.6	0.474	0.181	0.295	108	113	105	2.951
2010-05-15	8.4 5.0	0.313	0.131	0.183	107	112	103	2.437
2010-05-15	8.1 4.6	0.342	0.188	0.159	105	114	95	2.810
2010-05-15	8.1 5.0	0.371	0.138	0.235	104	113	99	2.296
2010-06-25	43.2 4.6	0.886	0.169	0.720	114	123	112	5.816
2010-06-25	43.2 5.0	0.780	0.143	0.637	113	118	111	5.302
2010-06-25	43.2 8.1	0.295	0.041	0.331	114	− 35	118	3.006
2010-06-25	43.2 8.4	0.309	0.033	0.339	119	− 38	121	2.865
2010-06-25	43.2 15.4	0.095	0.014	0.106	108	− 32	113	1.258
2010-06-25	43.2 23.8	0.090	0.026	0.108	90	− 39	101	0.566
2010-06-25	23.8 4.6	0.793	0.194	0.600	119	126	117	5.250
2010-06-25	23.8 5.0	0.741	0.168	0.573	122	122	122	4.736
2010-06-25	23.8 8.1	0.242	0.015	0.255	120	− 27	122	2.440
2010-06-25	23.8 8.4	0.216	0.007	0.223	124	− 34	124	2.299
2010-06-25	23.8 15.4	0.067	0.012	0.056	117	132	113	0.692
2010-06-25	15.4 4.6	0.698	0.182	0.519	115	125	112	4.558
2010-06-25	15.4 5.0	0.564	0.156	0.409	115	121	113	4.044
2010-06-25	15.4 8.1	0.162	0.027	0.185	112	− 36	116	1.748
2010-06-25	15.4 8.4	0.134	0.019	0.152	117	− 43	119	1.607
2010-06-25	8.4 4.6	0.484	0.201	0.285	120	126	115	2.951
2010-06-25	8.4 5.0	0.443	0.174	0.270	118	123	116	2.437
2010-06-25	8.1 4.6	0.417	0.208	0.212	120	128	113	2.810
2010-06-25	8.1 5.0	0.417	0.181	0.236	120	124	117	2.296
2010-08-01	23.8 4.6	0.698	0.173	0.525	115	113	116	5.250
2010-08-01	23.8 5.0	0.591	0.138	0.454	114	107	116	4.736
2010-08-01	23.8 15.4	0.085	0.009	0.080	135	80	140	0.692
2010-08-01	23.8 8.1	0.242	0.035	0.207	120	127	118	2.440
2010-08-01	23.8 8.4	0.201	0.013	0.188	117	102	118	2.299
2010-08-01	15.4 4.6	0.671	0.166	0.505	117	114	117	4.558

Table A4 – *continued*

Epoch	ν_1 ν_2	Δr_{12}	$r_1 - r_2$	$\Delta r_{\mathrm{core},\nu_1\nu_2}$	P.A.$_{\Delta r_{12}}$	P.A.$_{r_1-r_2}$	P.A.$_{\Delta r_{\mathrm{core},\nu_1\nu_2}}$	$\lambda_2 - \lambda_1$
	[GHz]	[mas]	[mas]	[mas]	[°]	[°]	[°]	[cm]
(1)	(2)	(3)	(4)	(5)	(6)	(7)	(8)	(9)
2010-08-01	15.4 5.0	0.552	0.130	0.421	112	109	113	4.044
2010-08-01	15.4 8.1	0.175	0.030	0.147	121	140	117	1.748
2010-08-01	15.4 8.4	0.134	0.006	0.128	117	135	116	1.607
2010-08-01	8.4 4.6	0.457	0.160	0.297	113	114	113	2.951
2010-08-01	8.4 5.0	0.379	0.125	0.254	108	108	109	2.437
2010-08-01	8.1 4.6	0.418	0.139	0.279	111	109	112	2.810
2010-08-01	8.1 5.0	0.313	0.106	0.208	107	101	110	2.296
2010-09-09	43.2 23.8	0.090	0.044	0.058	179	146	− 156	0.566
2010-09-09	23.8 4.6	0.631	0.073	0.642	115	− 149	109	5.250
2010-09-09	23.8 5.0	0.525	0.131	0.578	121	− 131	109	4.736
2010-09-09	23.8 8.1	0.268	0.032	0.263	117	− 167	110	2.440
2010-09-09	23.8 8.4	0.256	0.014	0.270	111	− 50	112	2.299
2010-09-09	23.8 15.4	0.060	0.033	0.085	90	− 40	107	0.692
2010-09-09	15.4 4.6	0.457	0.089	0.446	113	− 170	102	4.558
2010-09-09	15.4 5.0	0.433	0.136	0.456	124	− 145	106	4.044
2010-09-09	15.4 8.1	0.201	0.058	0.170	117	166	101	1.748
2010-09-09	15.4 8.4	0.124	0.019	0.111	104	147	97	1.607
2010-09-09	8.4 4.6	0.258	0.076	0.249	126	− 160	108	2.951
2010-09-09	8.4 5.0	0.162	0.130	0.158	158	− 137	110	2.437
2010-09-09	8.1 4.6	0.295	0.044	0.313	114	− 136	106	2.810
2010-09-09	8.1 5.0	0.234	0.107	0.287	130	− 121	109	2.296

This paper has been typeset from a TEX/LATEX file prepared by the author.